Surface Energy Balance Sensitivity to Meteorological Variability on Haig Glacier, Canadian Rocky Mountains

S. Ebrahimi and S. J. Marshall

Department of Geography, University of Calgary, 2500 University Drive, NW, Calgary, Alberta T2N 1N4, Canada

Correspondence to: S. Ebrahimi (samaneh.ebrahimi@ucalgary.ca)

Abstract

Energy exchanges between the atmosphere and the glacier surface control the net energy available for snow and ice melt. This paper explores the response of a mid-latitude glacier in the Canadian Rocky Mountains to daily and interannual variations in the meteorological parameters that govern the surface energy balance. We use an energy balance model to run sensitivity tests to perturbations in temperature, specific humidity, wind speed, incoming shortwave radiation, glacier surface albedo, and winter snowpack depth. Variables are perturbed (i) in isolation, (ii) including internal feedbacks, and (iii) with co-evolution of meteorological perturbations, derived from the North American regional climate reanalysis (NARR) over the period 1979-2014. Summer melt at this site has the strongest sensitivity to interannual variations in temperature, albedo, and specific humidity, while fluctuations in cloud cover, wind speed, and winter snowpack depth have less influence. Feedbacks to temperature forcing, in particular summer albedo evolution, double the melt sensitivity to a temperature change. When meteorological perturbations co-vary through the NARR forcing, summer temperature anomalies remain important in driving interannual summer energy balance and melt variability, but they are reduced in importance relative to an isolated temperature forcing. Covariation of other variables (e.g., clear skies, giving reduced incoming longwave radiation) may be partially compensating for the increase in temperature. The methods introduced in this paper provide a framework that can be extended to compare the sensitivity of glaciers in different climate regimes, e.g., polar, maritime, or tropical environments, and to assess the importance of different meteorological parameters in different regions.

1. Introduction

Glaciers and icefields are thinning and retreating in all of the world's mountain regions in response to global climate change (e.g., Marzeion et al., 2014). This is reshaping alpine environments, affecting regional water resources, and contributing to global sea level rise (e.g., Radić and Hock, 2011). A glacier's climate sensitivity can be expressed in terms of the energy or mass balance response to a change in meteorological conditions (Oerlemans and Fortuin, 1992; Oerlemans et al., 1998). For instance, Oerlemans et al. (1998) defined the static glacier sensitivity to temperature, S_T, i as:

$$S_T = \frac{\partial B_m}{\partial T} \approx \frac{B_m\,(+1K) - B_m\,(-1K)}{2} \tag{1}$$

where $B_m(\delta T)$ denotes the mean specific mass balance corresponding to the temperature perturbation δT. Mass balance sensitivity to precipitation perturbations, $S_P = \partial B_m / \partial P$, can be calculated in the same way.

Braithwaite and Raper (2002) extended the static sensitivity approach to regional scales, with the idea that glaciers within a given climate regime should have similar mass balance sensitivities to variations in temperature and precipitation. This framework has been used in numerous studies to describe glacier sensitivity to climate change (e.g., Dyurgerov 2001; Klok and Oerlemans, 2004; Arendt et al., 2009; Anderson et al., 2010; Engelhardt et al., 2015).

Most studies to date have concentrated on glacier mass balance response to changes in temperature and precipitation. This is sensible, as these are generally the most important meteorological variables affecting glacier mass balance. These two fields are also commonly measured, with long-term records available in many regions. Temperature and precipitation have also received the most attention because regional- to global-scale models of glacier mass balance commonly employ temperature-index methods to parameterize glacier melt (e.g., Marzeion et al., 2014; Clarke et al., 2015), with only these variables as inputs.

While temperature index models have demonstrated reasonable skill in estimating seasonal melt (Ohmura, 2001; Hock, 2005), they are nonetheless missing much of the physics that govern melt. Also, they may be overly sensitive to changes in temperature, without effectively capturing the impact of shifts in other variables such as wind, humidity, or cloud cover. Internal processes and feedbacks, such as surface albedo evolution, may also be absent, since degree-day melt factors are usually taken to be static. Such feedbacks are critical to glacier melt (e.g., Brock et al., 2000; Klok and Oerlemans, 2004; Cuffey and Paterson, 2010).

It is uncertain whether variability in glaciometeorological variables other than temperature and precipitation is important to glacier energy and mass balance. While most large-scale glacier change projections are rooted in temperature sensitivity (as built into temperature-index models), it is generally recognized that the complete surface energy balance is important to glacier melt. For instance, net radiation has been identified as the main source of melt energy for continental glaciers, accounting for ~70-80% of the total melt energy (e.g., Greuell and Smeets, 2001; Oerlemans and Klok, 2002; Klok et al., 2005; Giesen et al., 2008), with shortwave radiation providing the principal energy source. Incoming shortwave radiation is not directly dependent on

71 temperature. As another example, latent heat fluxes are a significant source of energy in maritime
72 and tropical environments (Wagnon et al., 1999, 2003; Favier et al., 2004; Anderson et al., 2010),
73 and their strength is a function of humidity and wind conditions, which are not strongly correlated
74 with temperature fluctuations. This calls for a broader exploration of glacier sensitivity to climate
75 variability and change, beyond just the influence of temperature.

76 Several studies that estimate glacier sensitivity to temperature change use complete models of
77 energy balance (e.g., Klok and Oerlemans, 2004; Klok et al., 2005; Anslow et al., 2008; Anderson
78 et al., 2010). The influence of other meteorological variables has been explored in a few studies.
79 Gerbaux et al. (2005) examine the role of different variables (e.g., temperature, moisture, wind) in
80 energy balance processes and climate sensitivity in the French Alps. Giesen et al. (2008) note the
81 importance of cloud cover in modulating interannual variability in summer melt on Midtdalsbreen,
82 Norway. Sicart et al. (2008) examine three glaciers in different latitudes/climate regimes.
83 Variations in net shortwave radiation, sensible heat flux, and temperature each contribute to
84 differences in glacier sensitivity to climate variability between these locations.

85 We build on these studies through a systematic examination of glacier energy balance and melt
86 sensitivity. We report the mean melt season conditions on Haig glacier in the Canadian Rocky
87 Mountains for the period 2002-2012. These reference data are used as a baseline for theoretical
88 and numerically modelled sensitivity. The same perturbation approach is then used to reconstruct
89 variations in surface energy balance and melt for the period 1979-2014, based on North American
90 regional climate reanalyses (NARR) (Mesinger et al., 2006). Our main question is whether
91 variables other than temperature and precipitation need to be considered to provide a realistic
92 estimate of glacier sensitivity to climate change for mid-latitude mountain glaciers. Our analysis
93 in this study is limited to just one site, with a focus on the summer melt season (vs. annual mass
94 balance). We examine the summer energy balance and evaluate the impact of different variables
95 in isolation and with more realistic covariance of meteorological conditions.

96

2. Surface Energy Balance and Melt Model

98 The energy budget at the glacier surface is defined by the fluxes of energy between the atmosphere,
99 the snow/ice surface, and the underlying snow or ice. The surface energy balance can be written
100

$$Q_N = Q_S^{\downarrow}(1 - \alpha) + Q_L^{\downarrow} - Q_L^{\uparrow} + Q_H + Q_E + Q_C, \qquad (2)$$

102

103 where Q_N is the net energy flux at the surface and $Q_S^{\downarrow}, Q_L^{\downarrow}, Q_L^{\uparrow}, Q_H, Q_E,$ and Q_C represent incoming
104 shortwave radiation, incoming and outgoing longwave radiation, sensible and latent heat flux, and
105 subsurface conductive energy flux, respectively. The energy fluxes have units of W m^{-2}. The
106 surface albedo is denoted α and fluxes are defined to be positive when they are sources of energy
107 to the glacier surface. We neglect the penetration of shortwave radiation and advection of energy
108 by precipitation and meltwater fluxes.
109

110 The net energy Q_N can be positive or negative. When it is negative, as it is for much of the winter
111 and during the night, the snow or ice will cool or liquid water will refreeze. Positive net energy

112 will drive surface warming, or on a melting glacier surface with $Q_N > 0$, the net energy flux is
113 dedicated to generating surface melt. For melt rate $\dot{m}$, this follows

$$\dot{m} = \frac{Q_N}{\rho_w L_f}, \tag{3}$$

117 where ρ_w is the density of water and L_f is the latent heat of fusion. Melt rates in Eq. (3) have units
118 of metres water equivalent per second (m w.e. s^{-1}).

120 Numerous studies have shown that incoming shortwave radiation is the dominant term in the
121 energy balance during the melt season in most glacial environments. Incoming shortwave radiation
122 (insolation) at the surface has three components: direct and diffuse solar radiation, along with
123 direct solar radiation that is reflected from the surrounding terrain. Direct solar radiation is the
124 radiative flux from the direct solar beam, which comes in at a zenith angle Z. It is a function of
125 latitude, time of year, and time of day (e.g., Oke, 1987). Potential direct (clear-sky) incoming solar
126 radiation on a horizontal surface can be estimated from

$$Q_\phi^\downarrow = Q_0 \cos(Z) \, \varphi_0^{P/P_0 \cos(Z)}, \tag{4}$$

130 for top-of-atmosphere insolation Q_0, clear-sky atmospheric transmissivity φ_0, air pressure P, and
131 sea-level air pressure P_0 (Oke, 1987). Eq. (4) allows potential direct shortwave radiation to be
132 calculated as a function of the day, year, latitude and elevation.

134 Longwave radiation can be estimated from the Stefan-Boltzmann equation,

$$Q_L = \varepsilon \sigma T^4, \tag{5}$$

138 where ε is the thermal emissivity, σ is the Stefan--Boltzmann constant, and T is the absolute
139 temperature of the emitting surface. Snow and ice emit as near-perfect blackbodies at infrared
140 wavelengths, with surface emissivity $\varepsilon_s = 0.98$-1.0. The longwave fluxes are then

$$Q_L^\uparrow = \varepsilon_s \sigma T_s^4, \tag{6}$$

143 and

$$Q_L^\downarrow = \varepsilon_a \sigma T_a^4, \tag{7}$$

146 for surface temperature T_s, near-surface air temperature T_a, and atmospheric emissivity ε_a. Terrain
147 emissions (i.e. from the surrounding topography) can also contribute to the incoming longwave
148 radiation, particularly at sites that are adjacent to valley walls.

150 A spectrally- and vertically-integrated radiative transfer calculation is needed to predict the
151 incoming longwave radiation from the atmosphere, as this depends on lower-troposphere water
152 vapour, cloud, and temperature profiles. Because the requisite atmospheric data are rarely available
153 in glacial environments, $Q_L^\downarrow$ is commonly parameterized at a site as a function of local (2-m)
154 temperature and humidity. Where available, cloud cover or a proxy for cloud conditions, such as
155 the atmospheric clearness index, are often used to strengthen this parameterization. Hock (2005)
156 and Lhomme et al. (2007) provide reviews of some of the parameterizations of atmospheric

157 emissivity that have been employed in glaciology. We found good results for regression-based
158 parameterization at two study sites in the Canadian Rocky Mountains (Ebrahimi and Marshall,
159 2015),

$$Q_L^\downarrow = (a + be_v + ch)\, \sigma T_a^4 \tag{8}$$

162 and

$$Q_L^\downarrow = (a + be_v + c\tau)\, \sigma T_a^4, \tag{9}$$

165 Here a, b, and c are regression parameters (different in Eqs. (8) and (9)), e_v is vapour pressure, h
166 is relative humidity, and τ is the clearness index, calculated from the ratio of measured to potential
167 direct incoming shortwave radiation.

169 Solar radiation and cloud data are less commonly available than relative humidity, so Eq. (8) is a
170 slightly less accurate but more portable version of this parameterization (Ebrahimi and Marshall,
171 2015). Multiple regressions of ε_a containing both relative humidity and clearness index were
172 rejected, as these are highly (negatively) correlated. All-sky longwave parameterizations using
173 either of these variables are reasonable, with root-mean square errors in mean daily incoming
174 longwave radiation of about 10 W/m^2.

176 Relative humidity can also be used as a proxy for clearness index if shortwave radiation data are
177 not available. Summer (JJA) observations at Haig Glacier follow the relation:

$$\tau = 1.3 - 0.01h\,, \tag{10}$$

181 for mean daily values of τ and h ($R^2 = 0.5$). We draw on this below when we need to estimate
182 perturbations in sky clearness index that are consistent with changes in atmospheric humidity. In
183 accord with the observational basis of Eq. (10), the clearness index is constrained to be within 0.3
184 and 1 ($h \in [30, 100\%]$); if daily mean humidity drops below this, we set $\tau = 1$.

186 Turbulent fluxes of sensible and latent energy in the glacier boundary layer are parameterized from
187 a bulk aerodynamic method (e.g., Andreas, 2002):

$$Q_H = \rho_a c_p k^2 v \left[\frac{T_a(z) - T_s}{\ln(^z/_{z_0})\ln(^z/_{z_{0H}})} \right], \tag{11}$$

191 and

$$Q_E = \rho_a L_v k^2 v \left[\frac{q_a(z) - q_s}{\ln(^z/_{z_0})\ln(^z/_{z_{0E}})} \right]. \tag{12}$$

194 Here ρ_a is the air density, c_p is the specific heat capacity of air, L_v is the latent heat of evaporation,
195 $k = 0.4$ is von Karman's constant, v is wind speed, and q refers to the specific humidity.
196 Measurements of temperature and humidity are assumed to be at two levels, height z (e.g., 2 m)
197 and at the surface-air interface, s. For a melting glacier surface, $T_s = 0°C$, and q_s can be taken from
198 the saturation specific humidity over ice at temperature T_s. We estimate T_s from an inversion of
199 Eq. (6), using measurements of outgoing longwave radiation. In sensitivity tests, where we depart

200 from the observational constraints, T_s is internally modelled within a subsurface snow model (see
201 below), taken from the temperature of the upper snow layer.
202
203 Parameters z_0, z_{0H}, and z_{0E} refer to the roughness length scales for turbulent exchange of
204 momentum, heat, and moisture. We adopt fixed values for each, equivalent for both snow and ice
205 ($z_0 = 3$ mm; $z_{0H} = z_{0E} = z_0/100$), based on closure of the surface energy balance with reference to
206 observed melt (Marshall, 2014). Atmospheric stability adjustments can be introduced in Eqs. (11)
207 and (12) to modify the turbulent flux parameterizations for the stable glacier boundary layer (e.g.,
208 Hock and Holmgren, 2005; Giesen et al., 2008). We do not apply stability corrections, as we are
209 able to attain closure in modelled and measured summer melt at this site without this. Others have
210 argued that stability corrections may lead to an underestimation of the turbulent fluxes on mountain
211 glaciers (e.g. Hock and Holmgren, 2005). This may be related to the low-level wind speed
212 maximum that is typical of the glacier boundary layer, which introduces strong turbulence and is
213 not consistent with the logarithmic profile of wind speed that is implicit in Eqs. (11) and (12). It
214 may also be that the effects of atmospheric stability are absorbed in the roughness values –
215 roughness values that are adopted to attain closure in the surface energy balance and melt
216 calculations may be too low, implicitly accounting for the stable boundary layer.
217
218 Subsurface temperatures are modelled through a multi-layer, one-dimensional model of heat
219 conduction and meltwater percolation and refreezing in the upper 10 m of the glacier, the
220 approximate depth of penetration of the annual temperature wave (Cuffey and Paterson, 2010).
221 This depth includes the time-varying seasonal snow layer and the underlying firn or ice. The
222 temperature solution follows
223

$$\rho_s c_s \frac{\partial T}{\partial t} = \frac{\partial}{\partial z}\left(-k_t \frac{\partial T}{\partial z}\right) + \varphi_t, \tag{13}$$

226 where ρ_s, c_s, and k_t are the density, heat capacity, and thermal conductivity of the subsurface snow,
227 firn, or ice and $\varphi_t(z)$ is a local source term that accounts for latent heat of refreezing,
228

$$\varphi_t = \rho_w L_f \dot{r}/\Delta z. \tag{14}$$

231 The refreezing rate $\dot{r}$ has units m s^{-1}, φ_t has units W m^{-3}, and Δz is the thickness of the layer in
232 which the meltwater refreezes.
233
234 Refreezing is calculated from a hydrological model that is coupled with the subsurface thermal
235 model. We track the volumetric liquid water fraction, θ_w, in the snow/firn pore space, and if
236 conductive energy loss occurs in a subsurface layer where liquid water is present, this energy is
237 diverted to latent enthalpy of freezing, rather than cooling the snow. Temperatures cannot drop
238 below 0°C until $\theta_w = 0$. Liquid water is converted to ice in the subsurface layer.
239
240 We model meltwater drainage by assuming that water percolates uniformly, with hydraulic
241 conductivity k_h and neglecting horizontal transport (i.e. assuming only gravity-driven vertical
242 drainage). Local water layer thickness can be expressed $h_w = \theta_w \Delta z$. The local water balance is then
243

$$\frac{\partial h_w}{\partial t} = -k_h \frac{\partial h_w}{\partial z} - \dot{r}, \tag{15}$$

245

246   where the final term accounts for water that is removed through internal refreezing. In principle,
247   this is a source/sink term that could also include internal melting (e.g., from shortwave radiation
248   penetration or percolation of warm rainwater), but we do not consider these processes. We assume
249   an irreducible water content of 3% for the melting snowpack (Colbeck, 1974), and the maximum
250   volumetric water content is equal to the porosity, θ, although drainage in the seasonal snowpack
251   is efficient and θ_w is always much less than θ.

252

253   *Numerical Energy Balance and Subsurface Temperature Model*

254

255   For the energy balance sensitivity experiments in this study, we use a combination of directly
256   observed and modelled glaciometeorological variables. Where we report the directly observed
257   surface energy balance, for the 2002-2012 reference state, we drive the energy balance model with
258   observed 30-minute data, including measured albedo and longwave radiation fluxes. Turbulent
259   heat fluxes and subsurface heat conduction are modelled from Equations (11-15).

260   Where we do sensitivity tests or run the model with other meteorological input, such as from
261   climate models, we need to allow for internal feedbacks such as freely-determined albedo
262   evolution and changes in incoming radiation that will attend changes in atmospheric conditions
263   (e.g., cloud cover, humidity). The energy balance and melt model that we employ is based on daily
264   mean meteorological inputs, in order to make our approach compatible with output from climate
265   models or reanalyses, as well as parameterizations that operate on a daily timescale (Eqs. 8-10). A
266   parameterized diurnal cycle is introduced for temperature and shortwave radiation (see below), in
267   order to capture the effects of overnight refreezing and the fraction of the day that experiences melt
268   (when Q_N and $T_s > 0$). The model uses a variable time step from 10 minutes to 1 hour to allow for
269   stability of the subsurface temperature prognosis.

270

271   The subsurface temperature model has 33 layers, with 10-cm layers until 0.6-m depth, 20-cm
272   layers from 0.6-2 m, and 40-cm layers from 2-10 m. The upper boundary forcing comes from the
273   conductive heat flux at the snow/ice-air interface, $Q_C = -k_t \partial T/\partial z$, modelled from a three-point
274   forward finite-difference approximation of $\partial T/\partial z$. We use a two-step solution, for the temperature
275   (Eq. 13), then the meltwater drainage (Eq. 15). The temperature solution is implicit for the
276   temperature diffusion, with latent heat release from refreezing (the source term in Eq. 13)
277   calculated from the previous time step within the hydrological model. Hydraulic conductivity in
278   Eq. (15) is assigned the value $k_h = 10^{-4}$ m s^{-1}, near the low end of estimates reported by Campbell
279   et al. (2006). Meltwater is assumed to drain instantaneously when it reaches the snow-ice interface.

280

281   The 10-m subsurface model consists of the seasonal snowpack of thickness $d_s(t)$, overlying either
282   firn or ice. The grid is fixed with respect to the surface, and each layer is assigned a density, thermal
283   conductivity, and heat capacity according to the medium (snow, firn, or ice). Snow and firn density
284   are modelled as a function of depth and the liquid water and ice content,

285

286    $$\rho_s = \rho_i(1 - \theta) + \rho_w\theta_w + \rho_i\theta_i , \qquad (16)$$

287

288   for porosity θ, liquid water fraction θ_w, and ice fraction θ_i. Densities ρ_s, ρ_i, and ρ_w refer to snow,
289   ice and water, respectively. We prescribe a decrease in porosity with depth following $\theta(z) = 0.6 -$

290   0.05z, parameterized to represent the measured summer snow densities at the site (ρ_s = 350-550
291   kg m^{-3}) and give reasonable estimates of firn density, up to ρ_s = 820 kg m^{-3} at 10-m depth.

292

293   Snow accumulates, melts, or undergoes densification on a daily time step, with snow thickness d
294   varying continuously (vs. discretely) within the fixed-grid framework. At depth d below the
295   surface, the grid cell has a weighted combination of thermal properties and densities to reflect the
296   mixture of snow and either firn or ice in that layer. We do not have a model for snow
297   accumulation through the winter months. We treat this simply, and linearly accumulate snow
298   from the start of winter until the start of the following melt season, with the accumulation rate set
299   to give a match to the observed May snowpack thickness for each year. These data are available
300   through annual winter mass balance surveys on the glacier, including a snowpit that provides
301   depth and density measurements at the AWS site.

302

303   The steps in the energy balance and melt model are as follows:

304

305   1. Daily mean values are input for temperature, incoming shortwave and longwave radiation, air
306   pressure, specific humidity, and wind speed, as well as minimum and maximum temperature.

307   2. A diurnal temperature cycle is parameterized as a cosine wave with a lag τ_t = 4 hours to give
308   the maximum temperature at 16:00, as per local observations, with an amplitude $A_t = (T_{max} - T_{min})/2$
309   (Figure 1a). For time t (hour of the day) and period P_t = 24 hours,

310
$$T(t) = -A_t \cos\left[\frac{2\pi(t-\tau_t)}{P_t}\right]. \tag{17}$$

311   3. A diurnal cycle for incoming shortwave radiation is parameterized as a half-cosine wave with
312   a period $P_{sw}(d) = 2h_s(d)$, where d is the day of year and h_s is the number of hours of sunlight on
313   day d (Figure 1b). Defining lag τ_{sw} and amplitude A_{sw},

314
$$Q_s^{\downarrow}(t) = \max\left\{-A_{sw}\cos\left[\frac{2\pi(t-\tau_{sw})}{P_{sw}}\right],0\right\}. \tag{18}$$

315   Sunlight hours are calculated as a function of latitude, θ, and day of year, based on the equation
316   for the sunset hour h_{ss} (e.g., Liou, 2002):

317
$$\cos(h_{ss}) = -\tan(\delta)\tan(\theta), \tag{19}$$

318   where δ is the solar declination angle (solar latitude as a function of day of year). Sunlight hours
319    $h_s = 2h_{ss}$. The lag also varies with the day of year, and is calculated by setting peak shortwave
320   radiation to occur at noon: $2\pi(12 - \tau_{sw})/P_{sw} = \pi$. This gives $\tau_{sw} = 12 - h_s$ hours. Amplitude A_{sw} is
321   calculated by integrating the area under the cosine curve and equating this to the average daily
322   incoming shortwave radiation, $Q_{Sd}^{\downarrow}$. This gives $A_{sw} = 12\pi\,Q_{Sd}^{\downarrow}/h_s$ W m^{-2}. This treatment implicitly
323   includes cloud effects that reduce incoming shortwave radiation on a given day (via $Q_{Sd}^{\downarrow}$), but
324   distributed evenly through the day. This neglects any systematic tendency for afternoon vs
325   morning clouds. For simplicity, we also neglect the effect of zenith angle on atmospheric
326   transmittance (i.e., lower transmittance for larger atmospheric path lengths in the morning and late
327   afternoon), although this could be built into a more refined model.

328   4. We assume that wind, incoming longwave radiation, air pressure, and specific humidity are
329   constant through the day, held to the mean daily value. For sensitivity tests, $Q_L^{\downarrow}$ is calculated
330   following Eq. (8) and the daily mean value of $Q_S^{\downarrow}$ is perturbed from Eq. (10) and $dQ_S^{\downarrow} = d\tau$.

331   5. Relative humidity has a diurnal cycle following temperature, assuming constant daily humidity
332   but adjusting h for consistency with the effect of temperature on saturation vapour pressure.

333   6. Albedo is also modelled on a daily basis for the sensitivity studies. When the seasonal snowpack
334   is melted away, albedo is set to the observed bare-ice value at the site, $\alpha_i = 0.25$. For fresh or dry
335   snow, a fixed value $\alpha_0 = 0.86$ is used. The snowpack thickness is initialized on May 1 of each year,
336   set to the observed value measured during the annual winter mass balance survey. During the melt
337   season, which is assumed to start after this date, seasonal snow albedo decreases as a function of
338   cumulative positive degree days ($\sum PDD$) following Hirose and Marshall (2013),

$$\alpha_s(d) = \alpha_0 - k_\alpha \sum PDD\,(d). \tag{20}$$

340   A minimum value of 0.4 is set for old snow. We parameterize the effects of summer snow fall on
341   albedo and mass balance through a stochastic model of summer precipitation events (Marshall,
342   2014). Precipitation events are set to occur randomly, with 25 events occurring from May through
343   September as the default setting. Precipitation totals vary randomly, between 1 and 10 mm w.e.,
344   with snow at temperatures below 0°C, rainfall above 2°C, and rain/snow partitioning increasing
345   linearly over the range 0-2°C. Following a summer snow event, surface albedo is reset to α_0, and
346   its albedo begins to decay following Eq. (20). This treatment allows a natural transition to end-of-
347   summer conditions, when fresh snowfall in September or October does not melt away.

348   7. Subsurface temperatures and the conductive heat flux, Q_C, are modelled with 10-minute to one-
349   hour time steps (chosen for stability of the temperature solution). The updated surface temperature
350   T_s is used for the calculation of outgoing longwave radiation (Eq. 6), sensible heat flux (Eq. 11),
351   and latent heat flux (via q_s in Eq. 12) for the next time step.

352   8. The hydrology model calculates meltwater drainage and refreezing. Annual meltwater runoff is
353   then the sum of all meltwater that drains, while summer mass balance is equal to the meltwater
354   runoff minus the total summer snowfall, nominally for the period May 1 to September 30 at this
355   site. This allows for some meltwater retention as either liquid water or refrozen ice within the snow
356   or firn. We neglect water storage in the englacial and subglacial hydrology systems.

357

358   ## 3. Field Site and Observational Data

359   Reference meteorological conditions, surface energy balance fluxes, and snow conditions are
360   based on *in situ* measurements at Haig Glacier in the Canadian Rocky Mountains for the period
361   2002-2012 (Marshall, 2014). Winter mass balance measurements are carried out each May. These
362   observations provide an 11-year record of observed snow depth and summer melt from an
363   automatic weather station (AWS) located near the median elevation of the glacier, 2660 m (Figure
364   2). This is the upper ablation area of the glacier, which generally undergoes a transition from
365   seasonal snow to exposed glacier ice in August.

Table 1 summarizes the mean observed meteorological and conditions at Haig Glacier over the 11-year reference period. Data coverage is incomplete, particularly in the winter months, as we transitioned to summer only measurements (May-Sept) after 2009. For the 11 years, data coverage is as follows for most sensors (e.g., temperature, shortwave radiation): JJA - 90% (909 of 1012 days); MJJAS – 86% (1441 of 1683 days); annual – 63% (2519 of 4018 days). There are more missing longwave radiation data, as the sensor was not installed until July 2003. The corresponding numbers are: JJA – 76%; MJJAS – 70%; annual – 46%.

Missing data are gap-filled from a weather station that has operated continuously in the glacier forefield since 2001, at an elevation of 2325 m. The forefield AWS has more complete data coverage than the glacier AWS, above 90% for all variables. Observational data are used to adjust for the altitudinal and environmental differences between the sites, through either a monthly offset (e.g., $T_G = T_{FF} - \Delta T$), or a scaling factor β (e.g., $v_G = \beta_v v_{FF}$). Here, subscripts G and FF refer to the glacier and forefield AWS sites. The monthly factors are calculated from the set of all available overlapping data for the two stations. The temperature offset approach is equivalent to a lapse rate, or can be expressed that way for distributed modelling over the glacier. In this study we consider only the point energy balance at the glacier AWS site. If both stations are missing data, gap-filling is done through assignment of mean daily observational data.

To give a sense of the complete data record, Figure 3 shows examples of the full record, for air temperature, modelled surface temperature, and the energy fluxes. Average June to August (JJA) air and surface temperature are 5.2°C and –0.6°C, respectively, and 98% of JJA days reach surface temperatures of 0°C (melting conditions) in the 11-year record. The surface energy fluxes in Fig. 3b illustrate the dominance of net radiation in governing net energy at this site (Table 2).

Mean daily values for the 11-year record are plotted in Figure 4. As is typical for mid-latitude glaciers, net radiation is the main energy flux that drives glacier melt at this site (Fig. 4c). Net radiation is negative in the winter, when shortwave inputs are low, albedo is high, and longwave cooling gives a radiation deficit. Net radiation is positive in the summer and increases through the melt season. This is driven by increases in net shortwave radiation as snow albedo declines at the site and then melts away to expose the underlying glacier ice (Fig. 4a). Measurements at the AWS site indicate a seasonal snow albedo decrease from about 0.8 to about 0.4 each summer, which may be due to a combination of increased snow water content, grain metamorphosis in the temperate snowpack, and increasing concentration of impurities through the melt season (e.g., Cuffey and Paterson, 2010).

Median daily melt rates for the period 2002-2012 are plotted in Fig. 4d, along with the interquartile range. On average, 65% of the annual glacier melt occurs in the months of July and August. Net energy peaks in August, when the low-albedo glacier ice is exposed. Sensible heat flux peaks in July, and is the other main source of energy contributing to glacier melt. On average for JJA, net radiation and sensible heat flux constitute 70% and 30% of the net energy, respectively. Latent heat flux represents a small sink of energy, and conductive heat flux is a minor source of energy.

The energy balance and snowpack models have been developed and tested elsewhere (Marshall, 2014; Ebrahimi and Marshall, 2015), so we do not present the model validation in detail here.

409   Comparisons are favorable between AWS observations (*e.g.*, in situ albedo, SR50-inferred melt),
410   the model driven with 30-minute AWS data, and the 'daily' version of the model used here, which
411   includes parameterizations of albedo, incoming longwave radiation, and the diurnal temperature
412   and shortwave radiation cycles (Section 2). The simplified daily model loses some reality, but its
413   overall performance is excellent.
414
415   As an example, glacier AWS data from summer 2015 is used as an independent test of the model,
416   with its default parameterizations. Observed melt at the AWS site was 3.1 ± 0.1 m w.e. in summer
417   2015, while the melt model forced by 30-minute AWS data gives 3.04 m w.e. and the
418   parameterized, daily version of the model gives 2.98 m w.e. Taking the 30-minute AWS-driven
419   results as the reference, the RMS error in the daily melt predictions for the parameterized model
420   is 3% (0.7 mm w.e., relative to a daily mean value of 22.7 mm w.e.). Departures from the
421   observations are primarily associated with the albedo, which is over-estimated in summer 2015.
422   Overall the parameterized daily model has good skill and is an appropriate tool for the sensitivity
423   analyses presented here.
424

4. Theoretical Sensitivity of the Surface Energy Balance

425
426
427   Surface energy balance processes and summer melt rates depend on various meteorological
428   influences (Eqs. 4-11). Warm summers generally cause high melt rates and promote negative mass
429   balance, but the energy balance is sensitive to other weather conditions as well. To examine these
430   sensitivities, meteorological variables in Tables 1 and 2 can be perturbed one at a time or in
431   combination to examine the impact on summer melt at the Haig Glacier AWS site. Perturbations
432   are introduced with respect to the mean JJA meteorological conditions from 2002-2012.

433   Theoretical sensitivities are calculated in this section by differentiating the net energy balance with
434   respect to each meteorological variable. This is akin to generating a Jacobian matrix for Q_N, based
435   on partial derivatives of the dependent variables in the surface energy balance. One cannot gauge
436   the most important meteorological influence on surface energy and mass balance from the
437   sensitivities to a unit change in each variable. For instance, a change in specific humidity of 1 g
438   kg^{-1} equals 3.3 standard deviations, with respect to the interannual (JJA) variability (Table 1). In
439   contrast, summer temperature has a standard deviation of 0.8°C, so a 1°C temperature change is a
440   smaller perturbation. To allow a direct comparison of the theoretical sensitivities and to give a
441   simple representation of their natural, interannual variability, we perturb each variable by one
442   standard deviation, based on the values reported in Tables 1 and 2.
443
444   We consider the core summer months, JJA, to calculate the theoretical sensitivity because the
445   glacier surface is at melting point for most of this time (Fig. 3a), which is a necessary condition to
446   relate net energy to melt. More than 80% of the annual melt also occurs in this season (Table 2
447   and Fig. 4d), so meteorological forcing over this period has the highest impact on glacier melt.

Sensitivity to Temperature

449   Air temperature appears directly in the expressions for $Q_L^{\downarrow}$ and Q_H. Temperature change may also
450   influence the surface energy balance through influences on other variables, such as atmospheric
451   moisture (Q_E). For a melting glacier surface, where surface and subsurface temperatures are at

452 0°C, air temperature changes do not directly influence $Q_L^\uparrow$ or Q_C. To estimate the magnitude of
453 temperature sensitivity, we differentiate each energy balance flux with respect to temperature.

455 For incoming longwave radiation, Eq. (7), the resulting temperature sensitivity is:

$$\frac{\partial Q_L^\downarrow}{\partial T} = 4\sigma\varepsilon_a T_a^3 + \sigma T_a^4 \frac{\partial\varepsilon_a}{\partial T} . \tag{21}$$

459 This general form applies to a range of formulations for ε_a, such as those of Brutsaert (1975),
460 Lhomme et al. (2007), or Sedlar and Hock (2009). Adopting the parameterization in Eq. (8), which
461 performs well at Haig Glacier,

$$\frac{\partial Q_L^\downarrow}{\partial T} = 4\sigma\varepsilon_a T_a^3 + \sigma T_a^4 \left(b\frac{\partial e_v}{\partial T} + c\frac{\partial h}{\partial T} \right) . \tag{22}$$

465 The last two terms reflect potential feedbacks of temperature change on humidity. While we are
466 only considering perturbations to temperature in this section, vapour pressure and relative humidity
467 cannot both remain constant under a temperature change. We first assume that relative humidity h
468 remains constant, under which conditions we assume that cloud cover and sky clearness will be
469 unchanged. For constant h, e_v scales with temperature following the Clausius-Clapeyon relation
470 for saturation vapour pressure,

$$\frac{\partial e_v}{\partial T} = \frac{h}{100}\frac{\partial e_s}{\partial T} = \frac{h}{100}\left(\frac{L_v e_s}{R_v T_a^2}\right) = \frac{L_v e_v}{R_v T_a^2} , \tag{23}$$

474 where $R_v = 461.5$ J kg^{-1} °C^{-1} is the gas law constant for water vapour.

476 For the mean JJA meteorological conditions at Haig Glacier, Eqs. (22) and (23) give $\partial Q_L^\downarrow/\partial T =$
477 4.7 W m^{-2} °C^{-1}. Temperature increases affect $Q_L^\downarrow$ through both the direct effect of higher emission
478 temperatures and the indirect effect of higher atmospheric emissivity, with these two terms in Eq.
479 (21) contributing 4.0 and 0.7 W m^{-2} °C^{-1}, respectively.

481 The temperature sensitivity of sensible and latent heat fluxes follow

$$\frac{\partial Q_H}{\partial T} = \frac{\rho_a c_p k^2 v}{\ln(^z/_{z_0})\ln(^z/_{z_{0H}})} , \tag{24}$$

485 and

$$\frac{\partial Q_E}{\partial T} = \frac{\rho_a L_p k^2 v}{\ln(^z/_{z_0})\ln(^z/_{z_{0E}})} \left(\frac{\partial q_v}{\partial T}\right) , \tag{25}$$

488 where

$$\frac{\partial q_v}{\partial T} \approx \frac{R_d}{PR_v}\left(\frac{\partial e_v}{\partial T}\right) , \tag{26}$$

491 for the dry gas-law constant $R_d = 289$ J kg^{-1} °C^{-1} and air pressure P, under the assumption that air
492 pressure and density are constant for small changes in temperature. Table 3 gives the turbulent

12

flux sensitivities for mean JJA conditions at Haig Glacier. Perturbations to both Q_H and Q_E are positive with an increase in temperature and the assumption of constant h. In combination with the increase in $Q_L^\downarrow$, net energy over the summer months is augmented by 12 W m^{-2} for a 1°C increase in temperature. Interannual variations in summer temperature (1σ) equal 0.8°C, giving a net energy perturbation $\delta Q_{N\sigma} = +10$ W m^{-2} (Table 3).

Fluctuations in energy balance can be related to melt rates through their combined influence on Q_N, with $\delta\dot{m} = \delta Q_N / \rho_w L_f$. Table 3 summarizes these impacts on summer melt, assuming a JJA melt season (92 days). The 1-σ temperature increase ($\delta Q_{N\sigma} = 10$ W m^{-2}) is equivalent to 236 mm of meltwater at the AWS site, a 10% increase over the reference JJA melt, 2320 mm w.e. These are the direct impacts of higher temperatures, not accounting for feedbacks or non-linearity in the seasonal evolution of melt conditions. These calculations assume that melting conditions prevail throughout the summer and all of this energy can be directed to snow/ice melt, which is not strictly true. We include them because estimates of the potential influence on summer melt provide an intuitive way to understand and compare sensitivities. We consider more realistic relations between net energy and melt in the modelled sensitivities of Section 5.

This initial scenario assumes that the warmer atmosphere contains more moisture, which is not necessarily the case. For instance, high summer temperatures in this region are commonly associated with ridging and subsidence, i.e. hot, dry conditions. If we assume that q_v is invariant with temperature (case 2 in Table 3), there is no feedback on the latent heat flux and the increase in net energy is less than with constant h: $\delta Q_{N\sigma} = 6.6$ W m^{-2} and $\delta m_\sigma = 157$ mm w.e.

However, there are additional feedbacks associated with relative humidity. If q_v is invariant, relative humidity must change to be consistent with the temperature perturbation. As an example, an increase of 1°C with no change in q_v corresponds to a decrease of 6% in mean summer h at our site, to 61%. This lowers the atmospheric emissivity in Eq. (8), reduces the incoming longwave radiation, and impacts $\partial\varepsilon_a/\partial T$ in Eq. (22). To be internally consistent, reduced humidity anomalies should also be associated with changes in cloud cover. For the 1°C temperature increase, the 6% decrease in relative humidity corresponds to an increase in clearness index of 0.06 (Eq. 10), from 0.63 to 0.69.

The effects of these radiation feedbacks are given in Table 3. Reduced relative humidity decreases $Q_L^\downarrow$ and increases $Q_S^\downarrow$. The resulting increase in shortwave radiation partially offsets the decline in $Q_L^\downarrow$, but there is an overall reduction in net radiation. For our parameterizations of the incoming radiation fluxes as a function of humidity, the effect of drier air on longwave radiation is stronger than the shortwave radiation feedback. This reduces the overall sensitivity to temperature change relative to the first two cases, with $\delta Q_{N\sigma} = 5.3$ W m^{-2} and $\delta m_\sigma = 125$ mm w.e. Note that these temperature scenarios are all idealized, neglecting albedo feedbacks and other indirect effects of a temperature change. These feedbacks are assessed in Section 5.

Sensitivity to Humidity and Wind

Similar derivatives and energy balance sensitivities can be derived with respect to the other meteorological variables, to explore the sensitivity of summer melt to different weather conditions. The sensitivity of sensible and latent heat fluxes to wind perturbations follow:

539

$$\frac{\partial Q_H}{\partial v} = \frac{\rho_a c_p k^2 (T_a - T_s)}{\ln(Z/z_0)\ln(Z/z_{0H})} \; , \qquad (27)$$

541

542 and

$$\frac{\partial Q_E}{\partial v} = \frac{\rho_a L_p k^2 (q_v - q_s)}{\ln(Z/z_0)\ln(Z/z_{0E})} \; , \qquad (28)$$

544

545 while the sensitivity to humidity is:

546

$$\frac{\partial Q_E}{\partial q_v} = \frac{\rho_a L_p k^2 v}{\ln(Z/z_0)\ln(Z/z_{0E})} \; . \qquad (29)$$

548

549 Incoming longwave radiation is also affected by perturbations in humidity, following:

550

$$\frac{\partial Q_L^{\downarrow}}{\partial q_v} = \sigma T_a^4 \frac{\partial \varepsilon_a}{\partial q_v} = \sigma T_a^4 \left(b \frac{\partial e_v}{\partial q_v} + c \frac{\partial h}{\partial q_v} \right). \qquad (30)$$

552

553 Table 3 summaries the theoretical sensitivities for specific humidity and wind perturbations of 1 g
554 kg^{-1} and 1 m s^{-1}, respectively, assuming that temperature is unchanged. For the humidity, we
555 present two scenarios: the first with perturbations to only the specific and relative humidity, and
556 the second including the expected effects of an increase in relative humidity on cloud cover.

557

558 Changes in humidity directly impact the latent heat flux, and may also influence incoming
559 longwave radiation and cloud cover (hence, incoming shortwave radiation). We consider the
560 effects of a humidity perturbation with and without radiative feedbacks in Table 3. For $\delta q_v = 1$ g
561 kg^{-1} and fixed temperature, mean summer relative humidity increases by 12%, to 79%, and Q_E
562 and Q_N increase by 10.5 W m^{-2}. Interannual variations in q_v equal 0.3 g kg^{-1}, giving $\delta Q_{N\sigma} = 3.2$ W
563 m^{-2}, corresponding to a 76-mm (3%) increase in summer melt.

564

565 Where radiation feedbacks are included, the increases in specific and relative humidity have a
566 strong influence on the atmospheric emissivity in Eq. (8), giving an increase in $Q_L^{\downarrow}$ of 24 W m^{-2}.
567 This is partially offset by cloud feedbacks associated with the increased humidity. Following Eq.
568 (10), $\delta h = 12\%$ equates to a decrease in atmospheric transmissivity of 0.11, which strongly
569 attenuates incoming shortwave radiation. This reduces the net radiation by 19 W m^{-2}, but the
570 radiation feedbacks remain positive. The net impact of a 1-σ humidity perturbation $\delta q_v = 0.3$ g kg^{-1}
571 is then 4.7 W m^{-2}, corresponding to a 112-mm (5%) increase in summer melt.

572

573 Wind perturbations have straightforward linear effects on Q_H and Q_E, giving a net sensitivity
574 $\partial Q_N / \partial v = +7$ W m^{-2} (m s^{-1})$^{-1}$. Sensible heat flux increases and evaporative cooling decreases
575 slightly. Winds have a low interannual variability at this site, 0.2 m s^{-1}, so the associated net energy
576 anomaly is $\delta Q_{N\sigma} = 2$ W m^{-2}, equivalent to 50 mm w.e. in summer melt.

577

578 *Sensitivity to the Radiation Fluxes*

579

580 Net shortwave radiation is affected by variations in top-of-atmosphere insolation, the clearness
581 index (i.e. cloud conditions), and surface albedo. Our functional relationship for net shortwave
582 radiation is $Q_{Snet} = Q_S^{\downarrow}(1-\alpha_S) = Q_{S\phi}\tau(1-\alpha_S)$, for potential direct insolation $Q_{S\phi}$ and clearness index
583 τ. From Eq. (4), sensitivity to top-of-atmosphere insolation Q_0 follows

$$\frac{\partial Q_{Snet}}{\partial Q_0} = \tau\,(1 - \alpha_S)\cos(Z)\,\varphi_0^{P/P_0\cos(Z)}, \tag{31}$$

587 An anomaly of 1 W m^{-2} in the top-of-atmosphere insolation, Q_0, gives $\delta Q_S^{\downarrow} = 0.6$ W m^{-2}, and the
588 net radiation impact is further reduced to 0.3 W m^{-2} by the surface albedo. The net impact of top-
589 of-atmosphere solar variability, such as sunspot cycles, is therefore small.

591 In contrast, incoming radiation fluxes and energy balance are strongly sensitive to atmospheric
592 transmissivity, which in turn is largely governed by cloud cover. Direct, independent variations in
593 incoming shortwave and longwave radiation are reported in Table 3 for fluctuations of 10 W m^{-2}
594 and for 1-σ variations in each. Sensitivity is moderate, of order 6% of the net energy.

596 It is more appropriate to consider co-variations of these radiation fluxes that can be expected in
597 association with changes in cloud cover. We can estimate through the sky clearness index, τ, as
598 parameterized via Eqs. (9) and (10), which relate the atmospheric emissivity and relative humidity
599 to clearness index. As an example, reduced cloud cover may be associated with a 1-σ increase in
600 τ of 0.1, from 0.63 to 0.73. This translates to an increase in net shortwave energy of 16 W m^{-2}
601 (Table 3), but the change in cloud cover also impacts incoming longwave radiation. Clearer skies
602 in the example of Table 3 give lower h, lower e_v, and lower $Q_L^{\downarrow}$. Latent heat flux also declines.
603 The overall result is a reduction in net energy for an increase in τ. A 1-σ increase (+0.04) gives a
604 3% reduction in net energy.

606 *Sensitivity to Albedo*

608 The sensitivity to albedo changes is comparatively high. An change in albedo of 0.1 creates an
609 energy balance perturbation of more than 100 W m^{-2} at local noon in mid-summer. The magnitude
610 of this effect varies with latitude, time of year, and atmospheric transmissivity. Integrated over the
611 daily solar path and over the summer, an albedo increase of 0.1 reduces net solar radiation by -23
612 W m^{-2}. Measurements at the site indicate an interannual albedo variability of 0.06, equivalent to
613 14% of the net energy or $\delta m_{\sigma} = -323$ mm w.e.

615 *Summary*

617 Overall, the results indicate a strong sensitivity of the summer energy balance and melt to
618 temperature and albedo, with weaker influences from cloud conditions, humidity, and wind speed.
619 These theoretical sensitivities are idealized, however, and neglect many important feedbacks and
620 glaciometeorological interactions that occur in glacier environments. The next two sections
621 examine the energy balance sensitivity at Haig Glacier within an energy balance-melt model. This
622 allows an estimate of feedbacks associated with the evolution of albedo, interannual variability in
623 weather conditions, and meteorologically-consistent covariance of weather variables.

5. Modelled Sensitivity of the Surface Energy Balance

We use a point model of surface energy balance, described in detail in Section 2. For all numerical experiments described below, we use the daily model with parameterizations of the longwave radiation fluxes, atmospheric clearness, diurnal cycles of temperature and shortwave radiation, and surface albedo evolution, following Eqs. (6), (8), (10), (17), (18), and (20). Surface temperature is modelled from the subsurface temperature model. The mean daily forcing for the energy balance and snowpack models is taken from the glacier AWS data, and the model is run year-round for the period 2002-2012. The May 1 snowpack thickness (winter accumulation) is specified for each year based on the measured winter mass balance at the AWS site.

Perturbations to the observed weather are used to repeat the sensitivity analyses of section 4, but with a realistic evolution of each summer melt season rather than the mean summer conditions. Meteorological variables are perturbed as follows: $\pm2°C$ for temperature, $\pm50\%$ for specific humidity and wind, ±0.1 for the sky clearness index (a proxy for cloud cover), and ±0.1 for albedo. Increments are set to give 41 realizations in each case, spanning the range of the perturbation. For example, temperature increments of 0.1°C are applied for the range -2 to 2°C. Each perturbation is prescribed for all days in the original data, and the energy balance program is run for the period 2002-2012. In each experiment, all other meteorological variables are held constant except for those that are direct impacted by a perturbation (e.g., relative humidity changes with temperature).

Table 4 lists the response of mean summer (JJA) net energy, Q_N, to the different meteorological perturbations. Changes in the energy fluxes can be examined in response to the perturbations, e.g., ΔQ_N as a function of temperature anomalies, δT. We plot these values to give sensitivity curves (e.g., Figures 5 and 6), and the slope of each curve is a measure of the sensitivity, e.g., dQ_N/dT. Values in Table 4 are calculated through linear regression. The relationships area generally nonlinear, so we compute the regressions for the region of the sensitivity curve within ±1 standard deviation ($\pm1\,\sigma$) of the reference value for each variable. This samples a more linear range and allows a better comparison with the derivatives in Table 3. Standard deviations refer to the interannual variability, as reported in Table 1. Table 4 also lists the change in net energy associated with a 1-σ increase in each variable.

There are multiple scenarios for temperature, shown in the first four cases in Table 4. These cases represent different assumptions about the way in which atmospheric moisture and radiation fluxes respond to a temperature perturbation. The first two cases follow the assumption that relative humidity does not change. Hence, a temperature change δT is attended by a change in specific humidity, δq_v, to maintain constant h. This impacts latent heat flux and atmospheric emissivity. Cases 1 and 2 show the net energy sensitivity to this scenario without and with albedo feedbacks. The next two cases include albedo feedbacks, but assume no change in specific humidity, $\delta q_v = 0$; hence relative humidity must respond. Cases 3 and 4 are without and with atmospheric radiation feedbacks to the changed relative humidity.

Summer melt sensitivity for the four different temperature perturbation scenarios is plotted in Figure 5. Case 1 lacks albedo feedbacks and corresponds to a net energy sensitivity of 13 W m^{-2} C^{-1}, which is comparable to the theoretical temperature sensitivities in Table 3. This is due to direct temperature/humidity impacts on incoming radiation fluxes, sensible heat flux, and latent heat flux.

Cases 2-4 include albedo feedbacks. This can be considered to be more realistic, and the albedo feedbacks have a roughly two-fold amplification effect on the temperature perturbation. Under constant h, $dQ_N/dT = 27$ W m^{-2} C^{-1} (cf. Figure 6a), representing a 28% increase in summer melt for a 1°C warming. This decreases by 6-10 W m^{-2} C^{-1} in cases 3 and 4, where q_v is held constant. Some of the reduced energy comes from the elimination of latent energy feedbacks. Case 4, with atmospheric radiation feedbacks, reduces energy further as decreased cloud cover (via higher τ) reduces incoming longwave radiation more strongly than it increases shortwave fluxes in the model. Here too, the numerical model gives a similar result to the theoretical prediction.

Figure 6a plots the response of the different surface energy fluxes for the reference model, case 2. Net shortwave radiation dominates the temperature response, over Q_H, Q_E, and $Q_L^{\downarrow}$. Figures 6b-6d provide similar details for perturbations in humidity, wind, clearness index, and albedo (cases 5-9 in Table 4). Sensitivity to humidity changes is relatively strong, through the combined impacts of latent and longwave fluxes (Fig. 6b). Case 6 is shown in this figure, including feedbacks on the atmospheric radiation. Incoming longwave radiation is strongly augmented by the increases in absolute and relative humidity, and accounts for about 70% of the net energy sensitivity to specific humidity. It is partially offset by cloud feedbacks, however, which reduce incoming shortwave radiation.

For increases in both temperature and humidity, the mean summer latent heat flux switches sign from negative (Table 2) to positive; that is, latent heat flux becomes a source rather than sink of energy under warmer and wetter conditions. In contrast, latent heat flux remains negative, but small, under increases in wind speed (Figure 6c). Energy balance sensitivity to wind perturbations is primarily associated with the sensible heat flux.

Net energy perturbations due to albedo and clearness index in Figure 6d are independent of each other, but are plotted together for convenience. Albedo sensitivity over the range ±0.1 is relatively high, with a decrease in net energy of 27 W m^{-2} (28%) for an increase in albedo of 0.1. Changes in sky clearness index (atmospheric transmissivity) have a lower impact, due to the compensating influences on incoming shortwave and longwave radiation. Reduced cloud cover (higher τ) gives an overall reduction in net energy at our site, as longwave radiation effects are dominant.

Sensitivity to Winter Snow Accumulation

Changes in the winter mass balance also influence the summer melt season. Interannual variability in the amount of snow is implicit in the simulations, as the spring (May 1) snowpack depth is initialized with the measured winter mass balance for each year, b_w (Marshall, 2014). However, these experiments do not control for the influence of snow depth on summer melt extent.

To examine this, we force the energy balance model over a range of winter mass balance conditions, $b_w \in [0.36, 2.36]$ m w.e. This is ±1 m w.e. relative to the mean observed value at the AWS site, 1.36 ± 0.27 m w.e. The melt model is run through 11 years of weather, 2002-2012, with the different values of winter mass balance as an initial condition. Figure 7 plots the average evolution of seasonal snowpack depth and albedo from May through September for this suite of experiments. Transitions from seasonal snow to ice span from early July to mid-September.

Albedo spikes in Fig. 7b are due to summer snow events, which become more frequent as temperatures cool in September.

The net energy balance perturbations that accompany these scenarios are shown for two choices of the minimum snow albedo (Fig. 7c). Observations of late-summer snow at the site are in the range 0.3-0.4, the two values presented here. The plot is asymmetric; net energy is more sensitive to reduced winter snow depths, which result in an earlier transition to exposed glacier ice. A 20% (1σ) reduction in b_w gives a net energy increase of about $4\,\mathrm{W\,m^{-2}}$ (4%), and the sensitivity increases non-linearly with increasingly lower snow depths. The influence from a deep winter snowpack is comparatively muted: $1\text{-}2\,\mathrm{W\,m^{-2}}$ reductions in Q_N for a 20% increase in the winter snow thickness. Perturbations in Q_N asymptote once seasonal snow is deep enough to survive through the summer.

The influence of the winter snowpack at this site is similar in magnitude to the net energy impacts of interannual variations in wind speed, but less important to the summer melt than observed variations in temperature, albedo, or cloud cover. This result is partly due to the relatively low contrast between late-summer snow albedo and bare-ice albedo at this site. If late-summer snow has a higher albedo, a deep winter snowpack is more effective at reducing the net energy and summer melt. The shape of the sensitivity curve would change for locations with higher-albedo snow, and also for sites in the lower ablation zone, where ice is exposed early in the melt season. A heavy winter snowpack would have a comparatively stronger role in this case. The result in Figure 7 is therefore more site-specific than for the other meteorological perturbations.

6. NARR-based Surface Energy Balance Reconstructions, 1979-2014

To examine energy balance sensitivity over a longer time period and with joint variation in meteorological variables, we run the energy balance model forced by North American Regional Reanalysis (NARR) atmospheric reconstructions from 1979 to 2014 (Mesinger et al., 2006). This provides a more complete picture of interannual variability, while comparison of NARR predictions with measurements over the period 2002-2012 also allows us to assess the skill with which fluctuations in surface energy balance and summer melt can be captured in an atmospheric model that does not explicitly resolve the alpine and glacier conditions.

We use a perturbation approach as in Section 5, taking NARR daily meteorological fields as anomalies relative to the mean NARR conditions for the period 2002-2012. Anomalies in near-surface temperature, specific humidity, wind speed, pressure, incoming shortwave radiation and incoming longwave radiation are used to drive the model for the 36-year period 1979-2014. Perturbations are introduced as anomalies relative to the mean observed conditions. NARR input fields allow us to introduce multiple perturbations at once, with magnitudes that are physically meaningful and meteorologically-consistent covariance of variables.

NARR has an effective spatial resolution of 32 km, and we extract mean daily data from the grid cell over Haig Glacier. This grid cell has an elevation of 2214 m, about 450 m lower than the AWS site. By using daily weather anomalies, we avoid most biases associated with the different altitude of the NARR grid cell. However, variations in some fields such as specific humidity, pressure, and temperature can be larger at lower elevations and over non-glacierized land surface types. Since we use meteorological fluctuations as perturbations, this is potentially problematic. Inspection of the summer variance in the different meteorological inputs over the reference period 2002-2012

761 indicates that this does not appear to be an issue. Standard deviations of each variable, calculated
762 from mean JJA values, are as follows: temperature, 0.8°C; specific humidity, 0.2 g kg^{-1}; wind
763 speed, 0.3 m s^{-1}; incoming shortwave radiation, 6 W m^{-2}; and incoming longwave radiation, 3 W
764 m^{-2}. Temperature, humidity, and wind values are equivalent to the observed range of variability
765 from 2002-2012 (Table 1), but the radiation fluxes are less variable. The effects of a lower
766 elevation in the NARR grid cell appear to be less than those associated with systematic biases in
767 the reanalysis, e.g., not enough variability in cloud conditions.

768 The energy balance model requires an estimate of winter snow accumulation. We base this on
769 cumulative NARR precipitation for the period September to May of each year, normalized to the
770 observed value of 1.36 m w.e. at the Haig Glacier AWS site. This permits interannual variability
771 in the winter snowpack thickness to be included in the simulations, by scaling the mean observed
772 value up or down based on the NARR winter precipitation totals. We use this as an initial condition
773 for the melt model (i.e., for May 1 snow depth).

774 We examine the sensitivity of net summer energy balance and melt to interannual variations in
775 each weather variable in the NARR forcing. Table 5 reports the NARR-based surface energy fluxes
776 and melt for JJA and MJJAS, averaged over the period 1979-2014. Mean values are all within 2
777 W m^{-2} of the reference surface energy fluxes (Table 2), derived from the in situ data, but there are
778 some significant differences in the standard deviation, which is a measure of the interannual
779 variability. As noted above, incoming shortwave radiation has about half of the variability in the
780 36-year NARR record as observed in the 11-year measurement period, and variance in incoming
781 longwave radiation is also less than observed. This implies more uniform summer cloud conditions
782 in the reanalysis, compared to the observational period.

783 Average summer albedo is also less variable in the model than the observations, and the mean
784 value in the NARR-forced model is too low for May through September (0.55 vs. an observed
785 value of 0.60). Most of this difference is associated with a low value of September albedo in the
786 model; we are generally underestimating September snow events and predicting too late a
787 transition from end-of-summer to the winter accumulation season. This transition occurs sometime
788 in September or October each year in our study period. September is mixed on the glacier, with
789 fresh snowfall alternating with periods of melting. This raises the average albedo on the glacier,
790 but our albedo parameterization does not fully capture this.

791 Figure 8a plots time series of the NARR-forced surface energy balance terms, and Figures 8b-8d
792 shows the relations between net energy and selected meteorological variables. These provide a
793 visual indication of the strength of each variable as a predictor of summer melt. Regressions
794 through these data points give estimates of net energy sensitivity, e.g. $\partial Q_N/\partial T$, as seen in actual
795 realizations of the summer weather conditions. These gradients can be thought of as the melt
796 sensitivity to interannual variability or trends in each weather variable.

797 The resulting sensitivities are given in Table 6, as well as linear correlation coefficients between
798 Q_N and all glaciometeorological variables that are used in the energy balance model. These
799 simulations are forced with NARR radiation flux anomalies, so we do not parameterize the
800 incoming longwave or shortwave radiation in these tests. The clearness index, τ, is not used, but it
801 can be calculated from the NARR relative humidity estimate, via Eq. (10), or more directly through

the fraction of incoming shortwave radiation relative to the clear-sky potential radiation. We test both approaches and find similar results. Values for $\partial Q_N/\partial \tau$ reported in Table 6 are averaged from the two approaches. We also report the direct relation between NARR total cloud cover and net energy; cloud cover is available in the reanalysis, but we do not have *in situ* data to compare with.

Temperature and albedo have the strongest influences on summer energy balance and melt. Fluctuations in specific humidity and incoming longwave radiation also correlate strongly with interannual variability in the summer energy budget. Wind speed, cloud conditions, and incoming shortwave radiation do not strongly contribute to the year-to-year variations in summer melt over the NARR period. There is a weak, positive relationship between the clearness index and net radiation in the NARR-forced results, indicating that increased shortwave radiation associated with reduced cloud cover has a stronger role than the associated reduction in longwave radiation.

These sensitivities can be compared with those in Section 5 (Table 4), but they differ in that the NARR forcing has multiple joint perturbations. This is realistic as the meteorological variables co-vary systematically, but it means that it is not possible to isolate the role of a single variable, such as temperature. A temperature change impacts several of the energy fluxes, but coincident changes in, e.g., humidity and radiation fluxes, may reinforce or reduce the temperature impacts. Results in Table 6 should therefore be interpreted as the 'net' or 'effective' influence of each weather variable on the summer energy balance, and some of them may have correlations that are more coincidental than casual. Most results are nonetheless similar in magnitude to the theoretical and modelling results (Tables 3 and 4), which are based on the *in situ* data. The largest exception is the relation between clearness index (cloud cover) and net energy, which is opposite in sign.

7. Discussion

We have taken three different approaches to estimate summer (JJA) energy balance and melt sensitivity at Haig Glacier: (i) theoretical, perturbing one variable at a time, (ii) a numerical model, restricting model experiments to single perturbations but allowing for internal feedbacks to be modelled, and (iii) through perturbations from a regional climate reanalysis, allowing multiple variables to change at once. Here we briefly summarize and interpret the integrated results from these different methods.

Haig Glacier Energy Balance Sensitivities and Feedbacks

Interannual variations in temperature and albedo have the strongest influence on summer energy balance in all three approaches to assessing Haig Glacier melt sensitivity (Figure 9). Fluctuations in humidity and longwave radiation are also important, while variations in cloud cover (τ), wind speed, and the winter snowpack thickness are less influential on the summer energy budget and melt extent at this site.

Temperature changes are generally thought of as the main driver of glacier advance and retreat, through combined influences on the surface energy budget, snow accumulation, and summer melt season. Sensitivities to temperature are commonly expressed as the change in summer or net mass

844 balance per unit warming. Sample mass balance sensitivities reported in the literature are −0.6 m
845 w.e. °C^{-1} on Morteratschgletscher, Switzerland (Klok and Oerlemans, 2004) and Illecillewaet
846 Glacier, British Columbia (Hirose and Marshall, 2013), −0.68±0.05 m w.e. °C^{-1} for a suite of
847 glaciers in Switzerland (Huss and Fischer, 2016), and −0.86 m w.e. °C^{-1} on South Cascade Glacier,
848 Washington (Anslow et al., 2008). Values as high as −2.0 m w.e. °C^{-1} are reported for Brewster
849 Glacier, New Zealand (Anderson et al., 2010).

851 These values are for the annual mass balance, but they are dominated by the summer melt response
852 to warming. They represent a melt sensitivity of about 30% °C^{-1} for the examples in the Alps and
853 western North America. When we introduce temperature perturbations in the absence of albedo
854 feedbacks, we find a relatively muted energy balance response, about 13 % °C^{-1}. The increase in
855 net energy is distributed about equally across the sensible heat flux, incoming longwave radiation,
856 and latent heat flux, and we have similar results for both the theoretical and numerically-modelled
857 temperature perturbations. Albedo feedbacks increase the net energy sensitivity to 28 % °C^{-1} or
858 −0.66 m w.e. °C^{-1}, in accord with previous studies. The exact number depends on assumptions
859 about humidity; if specific humidity increases with temperature (e.g., by holding relative humidity
860 constant), temperature sensitivity is higher.

862 The albedo feedback results from two main ways that temperature influences the seasonal albedo
863 evolution. A more intense melt season gives rise to a lower snow albedo and an earlier transition
864 from seasonal snow cover to glacial ice. We do not explicitly model impurities or snow-albedo
865 processes (e.g., grain metamorphosis, effects of snow-water content on the albedo), but we
866 parameterize the seasonal albedo evolution as a function of cumulative *PDD* (Eq. 20), which
867 makes the model directly sensitive to temperature perturbations.

869 Temperature changes have several additional, indirect impacts, including: (i) a longer melt season,
870 (ii) a greater fraction of time with surface temperatures at the melting point during the year, i.e.,
871 with reduced overnight cooling and refreezing, and (iii) an increase in the frequency of summer
872 rain vs. snow events. Summer snow events have an important impact on surface albedo, with fresh
873 snow strongly attenuating melt. Each of these processes contributes to the strong impact of
874 temperature anomalies on glacier melt. Combined with the albedo feedbacks, these processes and
875 help to explain why glaciers are strongly sensitive to temperature change.

877 Direct changes to albedo have an influence on summer energy balance and melt extent that is
878 comparable to the temperature influence, ~17% for a change in albedo equal to the interannual
879 albedo fluctuations, 0.06. Mean summer albedo differences arise as a feedback to other
880 meteorological forcings that drive the summer snow melt, but interannual albedo variations also
881 occur more directly, as a consequence of summer snowfall events, as a function of winter
882 accumulation totals, or due to impurity loading (e.g., black carbon deposition). The latter has been
883 observed in association with forest fires in British Columbia. Strong fire seasons occurred twice
884 during our period of study, in 2003 and 2015, and each left a measurably darker glacier surface.
885 For instance, the average albedo recorded at the AWS site in August 2003 was 0.13.

887 We found a relatively weak influence of winter mass balance on the summer melt extent. A low
888 snowpack depth has a greater impact, through an earlier transition to low-albedo bare ice. A deep
889 winter snowpack has the opposite influence, supporting a higher average summer albedo, but the

890 influence is weaker because the AWS site is in the upper ablation area, where the seasonal
891 snowpack persists until late summer in most years. The effects of greater winter accumulation
892 plateau once there is enough snow to survive the summer; beyond this point, additional snow has
893 no effect on the summer albedo or melt extent. Sensitivity to winter mass balance would likely be
894 stronger at lower altitudes on the glacier, and for the overall glacier mass balance.

896 Humidity changes can also be considered a feedback to temperature, but this is not certain; specific
897 humidity varies as a function of local- to synoptic-scale moisture sources and weather patterns,
898 and these are not necessarily coupled to temperature conditions. For instance, warm conditions at
899 Haig Glacier often accompany anticyclonic ridging in the summer months, during which time
900 southerly flows and upper-level subsidence promote dry, clear-sky conditions (low q_v and h). At
901 other times, westerly flows bring warm, moist Pacific air masses and humidity, temperature, and
902 cloud cover co-vary. Interannual variability in specific humidity has a significant impact on
903 summer energy and melt extent, an ~8% change for a perturbation of $0.3\,\mathrm{g\,kg^{-1}}$ (1σ). This effects
904 net energy through impacts on the latent heat flux and incoming longwave radiation. The latter is
905 partially compensated by accompanying changes in incoming shortwave radiation.

907 With all three methods, cloud cover shows up as a relatively weak influence on summer net energy
908 at this site, ~4% for a 1-σ variation in the clearness index (Figure 9). This result is a consequence
909 of the offsetting effects of cloud cover on the shortwave and longwave fluxes. The sign of the
910 relationship is also uncertain. In isolation, interannual fluctuations in shortwave and longwave
911 radiation have a moderate influence on the summer net energy (Figure 9), so these are important;
912 they are just not simply related to the cloud cover index, τ.

914 *NARR Results*

916 NARR results are broadly consistent with the *in situ*-based and theoretical sensitivities, in terms
917 of the relative importance of different meteorological parameters to interannual variability in
918 summer energy balance and melt. The influence of interannual temperature fluctuations appear to
919 be weaker than the other sensitivity experiments would suggest, ~15% °C^{-1}. All feedbacks
920 discussed above are active in the NARR-based simulations. The impacts of temperature variability
921 on net energy and melt could be partially compensated by other systematic changes in the energy
922 budget. For instance, warm temperatures are often associated with calm, clear-sky conditions that
923 reduce the incoming longwave radiation and the turbulent fluxes.

925 Temperature nonetheless emerges as the most important variable explaining interannual variations
926 in net energy. Mean summer net energy and temperature are highly correlated ($r = 0.84$). This
927 reinforces the argument that temperature indices offer a good proxy for net energy and summer
928 melt extent (e.g., Ohmura, 1987).

930 There are two other discrepancies in the NARR-forced results. Year-to-year variance in incoming
931 radiation fluxes is less than observed, pointing to poor representation of interannual cloud
932 variability in the reanalysis. The variability is still positively correlated with the in situ data (e.g.,
933 $r = 0.50$ for the correlation between incoming JJA shortwave radiation in NARR and in the data
934 from 2002-2012). Hence, NARR is picking up some of the observed variability, but it is muted.
935 The sensitivities to the radiation fluxes may still be representative, as there is still some interannual

variability for which on can assess the relation between Q_N and the radiation fluxes. However, the poor representation of the radiation fluxes and cloud conditions can be expected to reduce the skill of NARR-forced mass and energy balance reconstructions; this requires further study.

The other main difference with the NARR forcing is a switch in sign in the sensitivity to changes in cloud cover, as analyzed through either τ or the NARR-predicted total cloud cover. Clear-sky conditions have a positive relation with Q_N in the NARR-driven simulations, signalling that incoming shortwave radiation fluxes exert more influence than incoming longwave fluxes for net summer energy. Clear-sky conditions (less cloud cover) give increased shortwave radiation and a lesser decrease in longwave radiation, resulting in increased net energy. The theoretical and *in situ* sensitivities predict the opposite result, reduced net energy with clearer skies. The relationship is relatively weak, so it is possible that there are confounding variables in the NARR simulations once again, such as temperature effects masking the cloud relationship.

We do not test the ability and skill of NARR-forced energy and mass balance reconstructions here. This requires further study. In general, the perturbation method eliminates biases in the mean NARR variables, but a realistic representation of the variability and long-term trends in reanalysis fields is important to realistic representations of the glacier mas balance record and meltwater runoff. It would be instructive to analyze the synoptic weather patterns and weather anomalies in high-melt vs. low-melt summers in the NARR-driven simulations. We recommend an investigation of specific weather systems and their associated meteorological and energy balance conditions in followup work.

Representativeness of the Results

We have designed the sensitivity approach and the model to be applicable in regional studies, e.g. in a distributed model of glacier energy balance, forced by climate model reanalyses or projections. However, we did not expand our scope to other sites within the present study. In principle, the theoretical sensitivities (i.e. from the same set of equations) could be calculated for different baseline meteorological conditions, such as maritime or tropical environments. The method, rather than the specific Haig Glacier results, could be exported to other glacierized environments.

At regional scales, Haig Glacier energy balance sensitivities might be more transferrable, since similar summer climate conditions prevail across the Canadian Rocky Mountains (Ebrahimi and Marshall, 2015). Regional, multi-year reconstructions of glacier meltwater runoff might be feasible through a perturbation approach to summer mass balance, driven by meteorological anomalies from station data or climate models. This needs to be tested, however, for sensitive parameterizations such as the albedo model. It is uncertain whether the Haig glacier bare-ice and old-snow albedo are regionally representative.

Within Haig Glacier itself, our AWS site is in the upper ablation area, near the equilibrium ELA. Results are specific to the snow and ice albedo, snowpack depth, and meteorological/energy balance conditions at this location. We have not examined the representativeness of the results to other parts of the glacier, but summer melt extent and mass balance at the AWS site are strongly correlated with glacier-wide mass balance. We recommend additional work to calculate an average set of glacier sensitivities and assess whether the values presented here are representative. We

982 suspect that sensitivity of net energy to winter snow depth and the strength of albedo feedbacks
983 will vary across the glacier.
984
985 *Recommended Model Improvements*
986
987 Model improvements are recommended with respect to our treatment of the glacier surface albedo
988 and precipitation modelling. The energy balance, albedo, and melt models perform well in the core
989 summer melt season, June through August, when summer snowfall is infrequent and impacts on
990 the albedo are transient. We systematically underestimate September albedo, however; better
991 treatments of late-summer snow accumulation and the transition to the winter accumulation season
992 are needed.
993
994 Our meltwater drainage model is also simplistic. We assume that water drains efficiently from the
995 glacier surface, but in fact water has been observed to pond and refreeze on the surface. Re-melting
996 of this superimposed ice consumes energy and reduces the total summer runoff.
997
998 A more realistic treatment of year-round snow accumulation is also needed in order to carry out
999 model-based glacier mass balance reconstructions. We rely on observed winter mass balance for
1000 the studies here, but historical reconstructions and future projections require a way to reliably
1001 estimate snow accumulation from climate models. NARR precipitation in the Haig Glacier grid
1002 cell poorly represents the observed winter accumulation totals.
1003
1004 We have done tests to verify that the daily, parameterized model performs well relative to direct
1005 forcing with 30-minute AWS data, but some simplifications embedded in the daily model need to
1006 be examined. For instance, we assume constant cloud cover/clearness index over the day;
1007 systematic diurnal variations in cloud cover would affect the net radiation in ways that we do not
1008 capture. Overnight clouds serve to increase energy flux to the glacier, while daytime clouds reduce
1009 the incoming radiation. Effects like these become complicated to model or parameterize, but could
1010 bias our sensitivity results to cloud cover.
1011
1012 **8. Conclusions**
1013
1014 Sensitivity studies presented here extend the foundational work of Oerlemans and Fortuin (1992)
1015 and others, which has generally been done on glacier mass balance sensitivity to changes in
1016 temperature and precipitation. Our study is limited to summer mass balance at one location, but
1017 our results offer insight into the influence of different meteorological variables and energy fluxes,
1018 their year-to-year variability, and the role of isolated vs. collective forcings, feedbacks, and
1019 interactions on summer melt extent.
1020
1021 There is a good correspondence between the theoretical sensitivities and those derived from the
1022 numerical energy balance model, when feedbacks are omitted. This supports the potential
1023 application of the theoretical sensitivities to explore energy balance sensitivities under different
1024 climate regimes. This method can be transferred directly to other sites.
1025
1026 Temperature and albedo variations exert the strongest controls on year-to-year variability in
1027 summer melt at our site. While albedo can fluctuate independent of temperature, e.g., through the

influence of the winter snowpack depth or aerosol loading, it is also a powerful feedback mechanism to temperature and melt season evolution. In our model, albedo feedbacks give a two-fold increase in the net energy balance sensitivity to a temperature perturbation, amplifying the summer melt response from 13% $°C^{-1}$ to ~28% $°C^{-1}$. Temperature and albedo fluctuations are also the strongest influences on interannual melt variations in the NARR-forced surface energy balance, but the melt sensitivity to temperature variations is about 15% $°C^{-1}$, weaker than our result from the control experiments. This may be because the co-variation of other variables in the surface energy balance partially offsets the temperature forcing.

Humidity fluctuations are also effective in influencing the net energy, through their impacts on latent heat flux and incoming radiation fluxes. Wind speed, cloud conditions, and the winter snowpack thickness are less important to the summer energy balance and melt extent at our site. The relationship with cloud conditions is statistically weak and we do not have confidence in the sign; we recommend further work to assess the influence of cloud cover on summer net radiation at this site and elsewhere.

Our results suggest that it is may be reasonable to model glacier melt sensitivity at this site to temperature forcing, while ignoring variability and change in other weather conditions such as wind speed and cloud cover. This is the implicit premise in temperature-index melt models, and they can be tuned to work well at our site. We hesitate to recommend this though. Albedo feedbacks are crucial to include in assessments of glacier response to temperature change, and are not physically represented in most temperature-index models. Variations in humidity and their influence on melt are not negligible, and all terms in the surface energy budget contribute to the daily and interannual fluctuations in net energy.

Our modelling approach for surface energy balance is well-suited to a distributed energy balance model, applying the perturbation approach to larger scales (e.g., mountain ranges). Climate models simulate all of the relevant meteorological fields, and both past reanalyses and future projections can be driven using the perturbation approach introduced here. Meteorological sensitivities under different climate regimes (e.g., maritime, polar, or tropical conditions) can also be explored using this framework, to help understand regional differences in glacier sensitivity to climate variability and change.

Acknowledgements

References

Anslow, F.S., Hostetler, S., Bidlake, W.R. and Clark, P.U., Distributed energy balance modeling of South Cascade Glacier, Washington and assessment of model uncertainty. J. Geophys. Res.-Earth Surface., 113(F2), 2008.

Anderson, B., Mackintosh, A., Stumm, D., George, L., Kerr, T., Winter-Billington, A. and Fitzsimons, S.: Climate sensitivity of a high-precipitation glacier in New Zealand, J. Glaciol., 56(195), 114-128, 2010.

Andreas, E. L.: Parameterizing scalar transfer over snow and ice: a review, J. Hydrometeorol., 3, 417-432, 2002.

Arendt, A., Walsh, J. and Harrison, W.: Changes of glaciers and climate in northwestern North America during the late twentieth century, J. Climate, 22(15), 4117-4134, 2009.

Braithwaite, R.J. and Raper, S.C.: Glaciers and their contribution to sea level change, Phys. Chem. Earth, Parts A/B/C, 27(32), 1445-1454, 2002.

Braun, M. and Hock, R.: Spatially distributed surface energy balance and ablation modelling on the ice cap of King George Island (Antarctica), Global Planet. Change, 42, 45-58, 2004.

Brock, B. W., Willis, I. C., and Sharp, M. J.: Measurement and parameterisation of albedo variations at Haut Glacier d'Arolla, Switzerland, J. Glaciol., 46, 675-688, 2000.

Brutsaert, W.: On a derivable formula for long-wave radiation from clear skies, Water Resour. Res., 11, 742-744, 1975.

Campbell, F. M. A., Nienow, P. W. and Purves, R. S.: Role of the supraglacial snowpack in mediating meltwater delivery to the glacier system as inferred from dye tracer investigations, Hydrol. Process., 20, 969-985, 2006.

Clarke, G. K. C., Jarosch, A. H., Anslow, F. S., Radić V., and Menounos, B.: Projected deglaciation of western Canada in the twenty-first century, Nat. Geosci. 8, 372-377, 2015.

Colbeck, S. C.: The capillary effects on water percolation in homogeneous snow. Journal of Glaciology, 13(67), 85-97, 1974.

Cuffey, K. M., and Paterson, W. S. B.: The Physics of Glaciers, 4th Ed., Academic Press, Amsterdam, 2010.

Demuth, M.N., and Keller, R.: An assessment of the mass balance of Peyto Glacier (1966-1995) and its relation to recent and past-century climatic variability, In: Peyto Glacier: One Century of Science, National Hydrology Research Institute Science Report Series #8, Demuth, M.N., Munro, D.S., and Young, G.J., Environment Canada, Saskatoon, Sask., 83-132, 2006.

Dyurgerov, M.B.: Mountain glaciers at the end of the twentieth century: global analysis in relation to climate and water cycle, Polar Geog., 25(4), 241-336, 2001.

Ebrahimi, S., and Marshall, S. J.: Parameterization of incoming longwave radiation at glacier sites in the Canadian Rocky Mountains, J. Geophys. Res.-Atmos., in press, doi: 10.1002/2015JD023324, 2015.

Engelhardt, M., Schuler, T.V. and Andreassen, L.M.: Sensitivities of glacier mass balance and runoff to climate perturbations in Norway, Ann. Glaciol, 56(70), 79-88, 2015.

Favier, V., Wagnon, P., Chazarin, J. P., Maisincho L., and Coudrain, A..: One-year measurements of surface heat budget on the ablation zone of Antizana Glacier 15, Ecuadorian Andes, J. Geophys. Res.-Atmos. (1984-2012), 109, D18, doi: 10.1029/2003JD004359, 2004.

Gerbaux, M., Genthon, C., Etchevers, P., Vincent, C., and Dedieu, J. P.: Surface mass balance of glaciers in the French Alps: distributed modeling and sensitivity to climate change, Journal of Glaciology, 51, 561-572, 2005.

Giesen, R. H., Van den Broeke, M. R., Oerlemans, J., and Andreassen, L.M.: The surface energy balance in the ablation zone of Midtdalsbreen, a glacier in southern Norway: Interannual variability and the effect of clouds, J. Geophys. Res.-Atmos., 113, D21, doi:10.1029/2008JD010390, 2008.

Giesen, R. H., L. M. Andreassen, M. R. van den Broeke en J. Oerlemans: Comparison of the meteorology and surface energy balance on Storbreen and Midtdalsbreen, two glaciers in southern Norway. The Cryosphere, 2009, 3, 57-74, doi: 10.5194/tc-3-57-2009.

Greuell, W., and Smeets, P.: Variations with elevation in the surface energy balance of the Pasterze (Austria). J. Geophys. Res.-Atmos. (1984-2012), 106, D23, 31717-31727, 2001.

Hirose, J. M. R., and Marshall, S. J.: Glacier meltwater contributions and glacio-meteorological regime of the Illecillewaet River Basin, British Columbia, Canada, Atmos.-Ocean, 51, 416-435, doi:10.1080/07055900.2013.791614, 2013.

Hock, R.: Glacier melt: a review of processes and their modelling, Prog. Phys. Geog., 29, 362-391, 2005.

Hock, R. and Holmgren, B.: Some aspects of energy balance and ablation of Storglaciären, Sweden, Geografiska Annaler, 78A, 121-131, 1996.

Hock, R. and Holmgren, B.: A distributed surface energy-balance model for complex topography and its application to Storglaciären, Sweden, J. Glaciol., 51, 25-36, 2005.

Huss M. and Fischer M., Sensitivity of very small glaciers in the Swiss Alps to future climate change. Cryospheric Sciences. 2016:34.

Klok, E. J., and Oerlemans, J.: Model study of the spatial distribution of the energy and mass balance of Morteratschgletscher, Switzerland, J. Glaciol., 48, 505–518, 2002.

Klok, E. J. and Oerlemans, J.: Modelled climate sensitivity of the mass balance of Morteratschgletscher and its dependence on albedo parameterization, Int. J. Climatol, 24, 231-245, 2004.

27

Klok, E.J., Nolan, M. and Van den Broeke, M.R.: Analysis of meteorological data and the surface energy balance of McCall Glacier, Alaska, USA, J. Glaciol., 51(174), 451-461, 2005.

Lhomme, J. P., Vacher, J. J., and Rocheteau, A.: Estimating downward long-wave radiation on the Andean Altiplano, Agr. Forest Meteorol., 145, 139–148, 2007.

Liou, K.N.: An Introduction to Atmospheric Radiation, 2nd Ed. Academic Press, Amsterdam, 583 pp, 2002.

Marshall, S. J.: Meltwater runoff from Haig Glacier, Canadian Rocky Mountains, 2002–2013, Hydrol. Earth Syst. Sci., 18, 5181–5200, doi:10.5194/hess-18-5181-2014, 2014.

Marzeion, B., Cogley, J. G., Richter, K., and Parkes, D.: Attribution of global glacier mass loss to anthropogenic and natural causes, Science, 345, 919-921, 2014.

Mesinger, F., DiMego, G., Kalnay, E., Mitchell, K., Shafran, P.C., Ebisuzaki, W., Jovic, D., Woollen, J., Rogers, E., Berbery, E. H., and Ek, M. B.: North American Regional Reanalysis, Bull. Amer. Meteor. Soc., 87, 343-360, 2006.

Mölg, T., Cullen, N. J., Hardy, D. R., Kaser, G., and Klok, L.: Mass balance of a slope glacier on Kilimanjaro and its sensitivity to climate, International Journal of Climatology, 28, 881-892, 2008.

Oerlemans, J.: The mass balance of the Greenland ice sheet: sensitivity to climate change as revealed by energy-balance modelling. The Holocene, 1, 40-48, 1991.

Oerlemans, J. and Fortuin, J. P. F.: Sensitivity of glaciers and small ice caps to greenhouse warming, Science (New York, N.Y.), 258, 115-117, 1992.

Oerlemans, J., Anderson, B., Hubbard, A., Huybrechts, P., Johannesson, T., Knap, W.H., Schmeits, M., Stroeven, A.P., Van de Wal, R.S.W., Wallinga, J. and Zuo, Z.: Modelling the response of glaciers to climate warming, Clim. Dynam., 14(4), 267-274, 1998.

Oerlemans, J., and Klok, E. J.: Energy balance of a glacier surface: analysis of AWS data from the Morteratschgletscher, Switzerland. Arct. Antarct. Alp. Res., 34, 115-123, 2002.

Ohmura: Physical basis for the temperature-based melt-index method. J. Appl. Meteor., 40, 753–761, 2001.

Ohmura, A.: New temperature distribution maps for Greenland. Zeitschrift für Gletscherkunde und Glazialgeologie., 23 (1), 1-45, 1987.

Oke, T.R.: Boundary Layer Climates, 2nd Ed, Psychology Press, New York, 435, 1987.

Radić, V., and Hock, R.: Regionally differentiated contribution of mountain glaciers and ice caps to future sea-level rise, Nat. Geosci., 4, 91-94, 2011.

Sedlar, J., and Hock, R.: Testing longwave radiation parameterizations under clear and over-cast skies at Storglaciaren, Sweden, The Cryosphere, 3, 75–84, doi:10.5194/tc-3-75-2009, 2009.

1181   Shea, J. M. and S. J. Marshall. Synoptic controls on regional precipitation and glacier mass balance
1182   in the Canadian Rockies. International Journal of Climatology, 27 (2), 233-247, 2007.

1183   Sicart, J. E., Hock, R., and Six, D.: Glacier melt, air temperature, and energy balance in different
1184   climates: The Bolivian Tropics, the French Alps, and northern Sweden, J. Geophys. Res.,
1185   113, 2008.

1186   Sinclair, K. E. and S. J. Marshall. The impact of vapour trajectory on the isotope signal of Canadian
1187   Rocky Mountain snowpacks. J. Glaciol., 55 (191), 485-498, 2009.

1188   Wagnon P. W., Ribstein, P., Francou, B., and Pouyaud, B.: Annual cycle of energy balance of
1189   Zongo Glacier, Cordillera Real, Bolivia, J. Geophys. Res., 104, 3907-3923, 1999.

1190   Wagnon P. W., Sicart, J. E., Berthier, E., and Chazarin, J. P.: Wintertime high-altitude surface
1191   energy balance of a Bolivian glacier, Illimani, 6340 m above sea level, J. Geophys. Res.,
1192   108 (D6 4177), doi:10.1029/2002JD002088, 2003.

1193   Willis, I. C., Arnold, N. S., and Brock, B. W.: Effect of snowpack removal on energy balance, melt
1194   and runoff in a small supraglacial catchment, Hydrol. Process., 16, 2721-2749, 2002.

1195   WGMS: World Glacier Monitoring Service, Zurich, Switzerland. Glacier Mass Balance Bulletins
1196   (M. Zemp et al., Eds.), ICSU(WDS)/IUGG(IACS)/UNEP/UNESCO/WMO, data available
1197   at http://wgms.ch/gmbb.html, 2014.

Tables

Table 1. Mean monthly weather conditions ± one standard deviation at Haig Glacier, Canadian Rocky Mountains, May to September 2002-2012. Data are from automatic weather station measurements at an elevation of 2660 m, in the upper ablation zone of the glacier.

Month	T (°C)	h (%)	e_v (hPa)	q_v (g/kg)	P (hPa)	v (m/s)
May	−1.4 ± 1.1	73 ± 4	4.0 ± 0.4	3.4 ± 0.4	743.0 ± 2.4	2.8 ± 0.2
June	2.6 ± 0.9	73 ± 6	5.5 ± 0.5	4.6 ± 0.4	748.1 ± 1.4	2.6 ± 0.2
July	6.9 ± 1.4	62 ± 5	6.4 ± 0.4	5.3 ± 0.3	751.2 ± 1.6	2.8 ± 0.3
August	5.9 ± 1.1	64 ± 7	6.1 ± 0.4	5.1 ± 0.4	750.8 ± 1.4	2.5 ± 0.2
Sept	2.1 ± 1.8	71 ± 10	5.0 ± 0.4	4.2 ± 0.3	748.4 ± 1.8	3.0 ± 0.4
JJA	5.1 ± 0.8	67 ± 4	5.7 ± 0.4	4.8 ± 0.3	750.0 ± 1.1	2.6 ± 0.2
MJJAS	3.2 ± 0.7	69 ± 4	5.3 ± 0.3	4.3 ± 0.3	748.3 ± 1.4	2.7 ± 0.2

Table 2. Mean monthly surface energy balance terms ± one standard deviation at Haig Glacier, Canadian Rocky Mountains, May to September 2002-2012. Radiation fluxes and albedo values are from automatic weather station measurements and the turbulent fluxes and subsurface heat conduction are modelled from the AWS data. Fluxes are in W m^{-2} and melt totals are in m w.e.

Month	$Q_S^{\downarrow}$	α_s	$Q_L^{\downarrow}$	$Q_L^{\uparrow}$	Q_H	Q_E	Q_C	Q_N	melt
May	249 ± 24	0.76 ± 0.04	258±12	299±4	7±4	−11±3	5±2	22±12	0.20±0.10
June	237 ± 23	0.70 ± 0.05	276±14	310±2	17±4	−5±4	3±1	56±21	0.45±0.16
July	240 ± 19	0.57 ± 0.06	275±8	313±1	38±9	1±5	1±1	109 ±27	0.88±0.21
August	205 ± 25	0.38 ± 0.07	273±11	312±1	32±7	−1±3	2±1	123 ±22	0.99±0.18
Sept	140 ± 30	0.59 ± 0.09	271±13	306±3	23±12	−6±3	3±2	42 ±21	0.34±0.16
JJA	227 ± 14	0.55 ± 0.06	275±6	312±1	29±3	−2±3	2±1	97 ±19	2.32±0.45
MJJAS	215 ± 17	0.60 ± 0.04	271±7	308±1	23±4	−4±3	3±1	71 ±15	2.86±0.59

Table 3. Surface energy balance sensitivity to meteorological perturbations over a melting glacier surface, from direct feedbacks only. Calculations are for mean JJA conditions at Haig Glacier. All energy flux perturbations are expressed in $W\,m^{-2}$. $\delta Q_{N\sigma}$ is the net energy perturbation for a 1-σ increase in the variable. The melt perturbation, δm_σ, has units of mm w.e., and is calculated assuming that $\delta Q_{N\sigma}$ holds for JJA (92 days).

Perturbation	$\delta Q_S^\downarrow$	$\delta\alpha$	δQ_S^{net}	$\delta Q_L^\downarrow$	δQ_H	δQ_E	δQ_N	$\delta Q_{N\sigma}$	δm_σ
$\delta T = 1°C$; $\delta h=0$	0	0	0	4.7	4.2	3.5	12.4	9.9	236
$\delta T = 1°C$; $\delta q_v=\delta\tau=\delta\varepsilon_a=0$	0	0	0	4.0	4.2	0	8.3	6.6	157
$\delta T = 1°C$; $\delta q_v=0$; $\delta\tau, \delta\varepsilon_a$	22.6	0	10.2	−7.8	4.2	0	6.6	5.3	125
$\delta q_v = 1\ g\ kg^{-1}$; $\delta\tau=\delta\varepsilon_a=0$	0	0	0	0	0	10.5	10.5	3.2	76
$\delta q_v = 1\ g\ kg^{-1}$; $\delta\tau, \delta\varepsilon_a$	−41.8	0	−18.8	24.1	0	10.5	15.7	4.7	112
$\delta v = 1\ m\ s^{-1}$	0	0	0	0	8.3	−1.4	6.9	2.1	50
$\delta Q_0 = 1\ W\,m^{-2}$	0.6	0	0.3	0	0	0	0.3	−	−
$\delta Q_S^\downarrow = 10\ W\,m^{-2}$	10.0	0	4.5	0	0	0	4.5	6.3	150
$\delta Q_L^\downarrow = 10\ W\,m^{-2}$	0	0	0	10	0	0	10.0	6.0	143
$\delta\tau = 0.1$	36.0	0	16.2	−19.6	0	−4.6	−8.0	−3.2	−76
$\delta\alpha_S = 0.1$	0	0.1	−22.7	0	0	0	−22.7	−13.6	−323

Table 4. Net energy balance sensitivity to meteorological perturbations in the surface energy balance model, based on regressions to the sensitivity curves (cf. Figure 6). Also shown is the change in net energy associated with a 1-σ increase in each parameter, averaged over JJA.

Perturbation	Sensitivity	δQ_N for +1σ
1. $\delta T = \pm 2°C$; $\delta h=0$; $\delta\alpha_S=0$	$\partial Q_N/\partial T = 13\ W\,m^{-2}\,(°C)^{-1}$	$+10\ W\,m^{-2}$
2. $\delta T = \pm 2°C$; $\delta h=0$	$\partial Q_N/\partial T = 27\ W\,m^{-2}\,(°C)^{-1}$	$+21\ W\,m^{-2}$
3. $\delta T = \pm 2°C$; $\delta q_v=\delta\tau=\delta\varepsilon_a = 0$	$\partial Q_N/\partial T = 21\ W\,m^{-2}\,(°C)^{-1}$	$+17\ W\,m^{-2}$
4. $\delta T = \pm 2°C$; $\delta q_v=0$; $\delta\tau, \delta\varepsilon_a$	$\partial Q_N/\partial T = 17\ W\,m^{-2}\,(°C)^{-1}$	$+13\ W\,m^{-2}$
5. $\delta q_v = \pm 50\%$; $\delta\tau, \delta\varepsilon_a = 0$	$\partial Q_N/\partial q_v = 15\ W\,m^{-2}\,(g/kg)^{-1}$	$+5\ W\,m^{-2}$
6. $\delta q_v = \pm 50\%$; $\delta\tau, \delta\varepsilon_a$	$\partial Q_N/\partial q_v = 25\ W\,m^{-2}\,(g/kg)^{-1}$	$+8\ W\,m^{-2}$
7. $\delta v = \pm 50\%$	$\partial Q_N/\partial v = 14\ W\,m^{-2}\,(m/s)^{-1}$	$+3\ W\,m^{-2}$
8. $\delta\tau = \pm 0.1$	$\partial Q_N/\partial\tau = -9\ W\,m^{-2}\,(0.1)^{-1}$	$-4\ W\,m^{-2}$
9. $\delta\alpha_S = \pm 0.1$	$\partial Q_N/\partial\alpha_S = -27\ W\,m^{-2}\,(0.1)^{-1}$	$-16\ W\,m^{-2}$
10. $\delta b_w = \pm 1\ m\,w.e.$	$\partial Q_N/\partial b_w = -12\ W\,m^{-2}\,(m\ w.e.)^{-1}$	$-3\ W\,m^{-2}$

1287
1288
1289
1290
1291
1292
1293
1294
1295
1296
1297
1298
1299
1300
1301
1302
1303
1304
1305
1306
1307
1308
1309
1310
1311
1312
1313
1314
1315
1316
1317
1318
1319
1320

Table 5. Summer surface energy balance fluxes on Haig Glacier as forced by the North American Regional Reanalysis (NARR) daily weather fields, 1979-2014. NARR inputs are taken as perturbations to the mean observed values. Melt is in m w.e., and all fluxes have units W m^{-2}.

Period	$Q_S^{\downarrow}$	α_s	$Q_L^{\downarrow}$	$Q_L^{\uparrow}$	Q_H	Q_E	Q_C	Q_N	melt
JJA	227 ± 7	0.53 ± 0.05	275 ± 4	311 ± 1	27 ± 4	-3 ± 3	2 ± 1	95 ± 14	2.28 ± 0.42
MJJAS	215 ± 6	0.55 ± 0.04	271 ± 4	308 ± 2	22 ± 3	-5 ± 3	3 ± 1	73 ± 10	2.68 ± 0.50

Table 6. Correlation and sensitivity of different weather variables to the mean summer (JJA) net energy flux, Q_N, for the NARR simulations, 1979-2014. 'cloud' is the NARR total cloud fraction.

| Variable	Correlation	Sensitivity	δQ_N for $+1\sigma$
$T\,(°C)$	0.84	$\partial Q_N / \partial T = 14\ \text{W m}^{-2}\,(°C)^{-1}$	$+10\ \text{W m}^{-2}$
$q_v\,(\text{g kg}^{-1})$	0.50	$\partial Q_N / \partial q_v = 25\ \text{W m}^{-2}\,(\text{g/kg})^{-1}$	$+7\ \text{W m}^{-2}$
$v\,(\text{m s}^{-1})$	0.00	$\partial Q_N / \partial v = -4\ \text{W m}^{-2}\,(\text{m/s})^{-1}$	$-1\ \text{W m}^{-2}$
$Q_S^{\downarrow}\,(\text{W m}^{-2})$	0.14	$\partial Q_N / \partial Q_S^{\downarrow} = 0.3\ \text{W m}^{-2}\,(\text{W m}^{-2})^{-1}$	$+2\ \text{W m}^{-2}$
$Q_L^{\downarrow}\,(\text{W m}^{-2})$	0.64	$\partial Q_N / \partial Q_L^{\downarrow} = 2\ \text{W m}^{-2}\,(\text{W m}^{-2})^{-1}$	$+8\ \text{W m}^{-2}$
τ	0.25	$\partial Q_N / \partial \tau = 15\ \text{W m}^{-2}\,(0.1)^{-1}$	$+4\ \text{W m}^{-2}$
cloud	-0.19	$\partial Q_N / \partial c = -8.1\ \text{W m}^{-2}\,0.1)^{-1}$	$-3\ \text{W m}^{-2}$
α_S	-0.83	$\partial Q_N / \partial \alpha_S = -26\ \text{W m}^{-2}\,(0.1)^{-1}$	$-11\ \text{W m}^{-2}$
$b_w\,(\text{m w.e.})$	-0.15	$\partial Q_N / \partial b_w = -3\ \text{W m}^{-2}\,(\text{m w.e.})^{-1}$	$-1\ \text{W m}^{-2}$
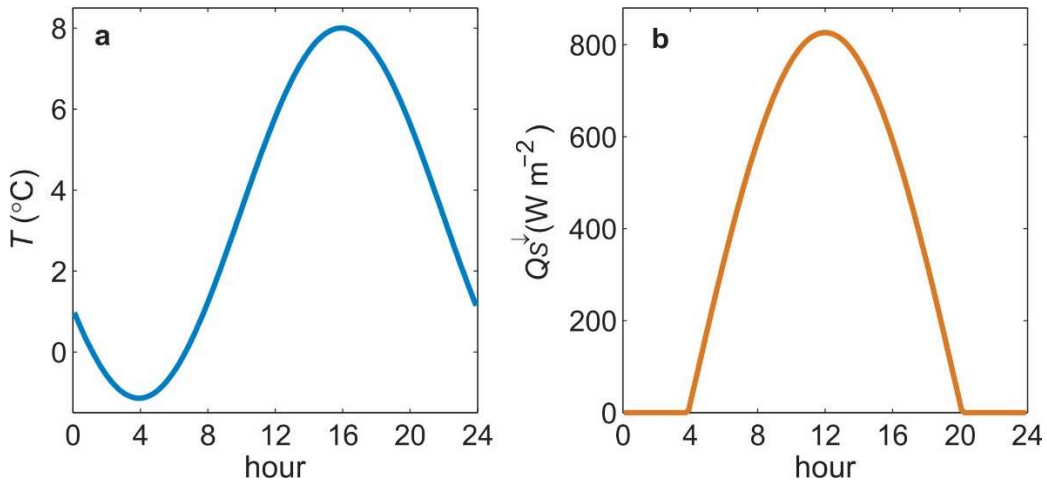
Figures

1323

1324 **Figure 1.** Idealized diurnal cycles of (a) temperature and (b) incoming shortwave radiation used
1325 in the energy balance model. These two examples are for a sample day, July 1, 2010, parameterized
1326 from daily minimum and maximum temperature in (a) and day of year plus mean daily incident
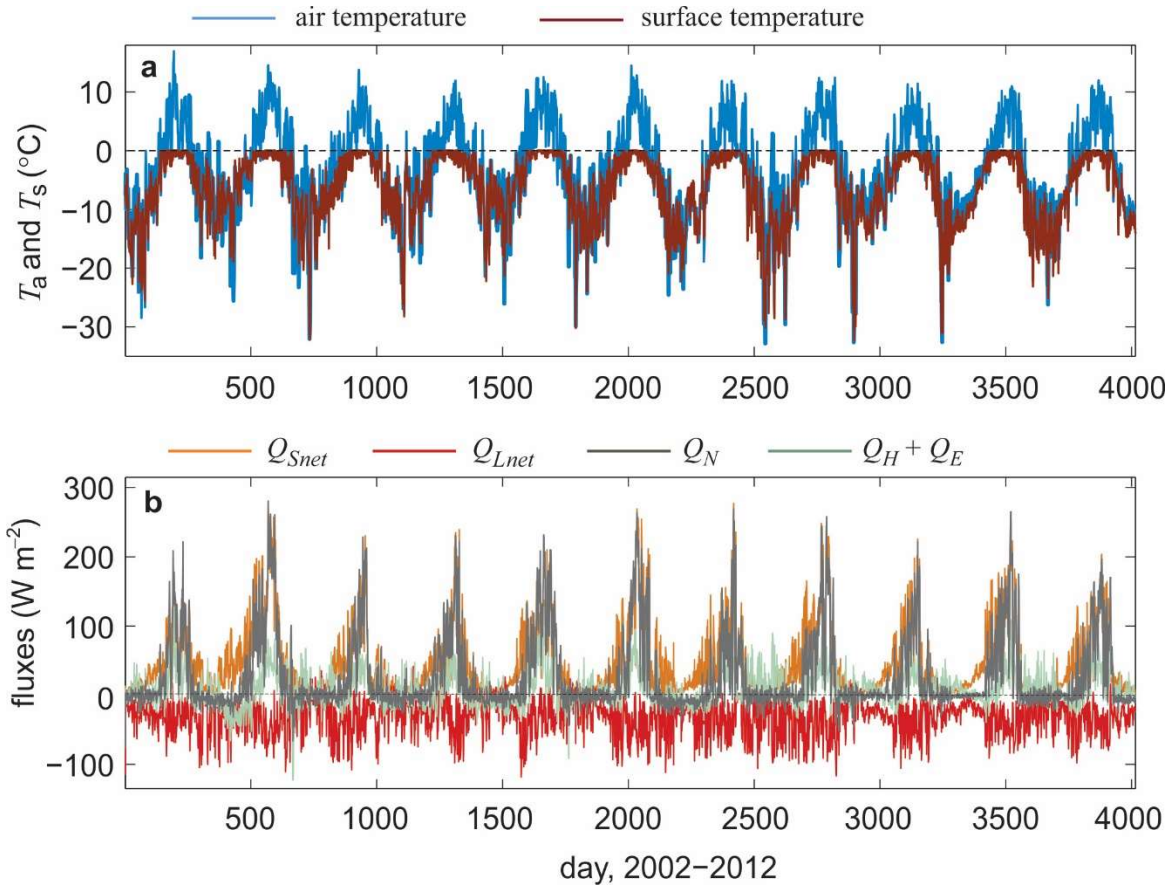1327 shortwave radiation in (b).

1328

1329
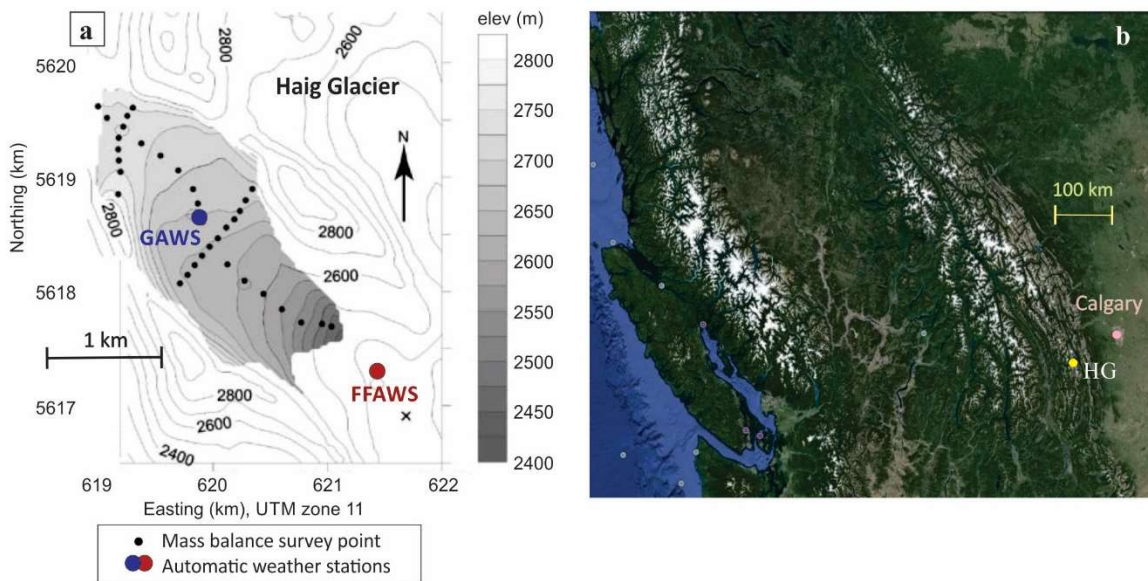
1330

1331

1332 **Figure 2.** (a) The topography and automatic weather stations on Haig Glacier (GAWS) and the
1333 glacier forefield (FFAWS). The smaller black dots are mass balance survey points. (b) The
1334 location of Haig Glacier is labelled HG on the Google Earth map of southwestern Canada.

1335
1336
1337
1338
1339

1340
1341
1342 **Figure 3.** The 11-year record of (a) air temperature, modelled surface temperature, and (b) surface
1343 energy fluxes at the Haig Glacier AWS site. Daily mean values are plotted from Jan 1, 2002-Dec
1344 31, 2012.

1345
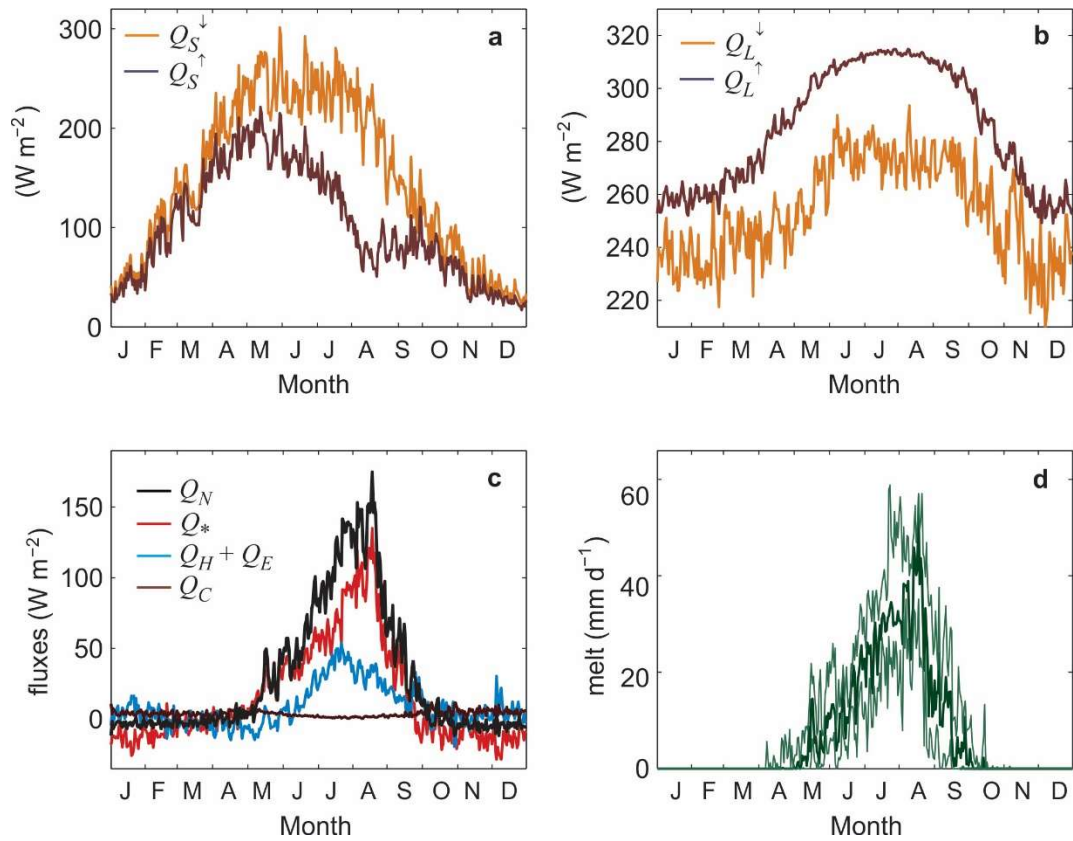
1346

Figure 4. The average annual cycle of (a-c) surface energy fluxes and (d) daily melt at the Haig
Glacier AWS. Daily mean values are plotted for the period 2002-2012. For melt rates, the heavy
line is the median value and the thin lines indicate the interquartile range.

1350
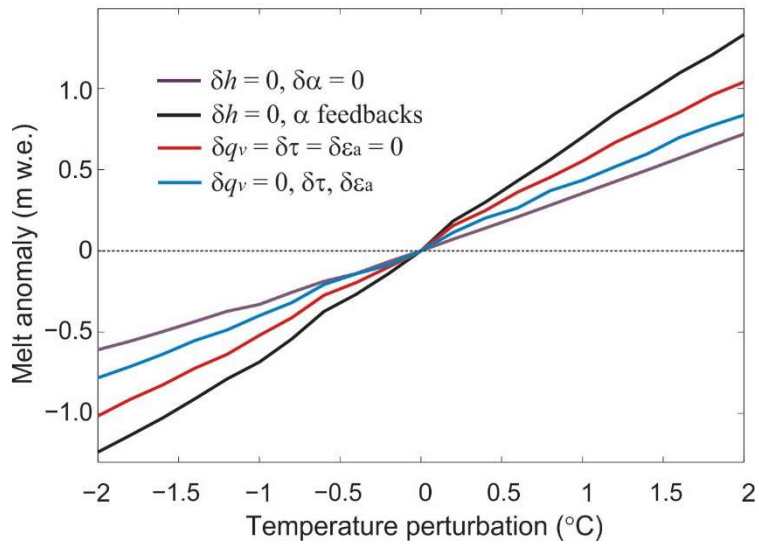
1351
1352
1353
1354   **Figure 5**. Sensitivity of modelled summer (JJA) melt to temperature perturbations for different
1355   assumptions, as per Table 4. The reference (mean 2002-2012) JJA melt is 2.32 m w.e.
1356

1357
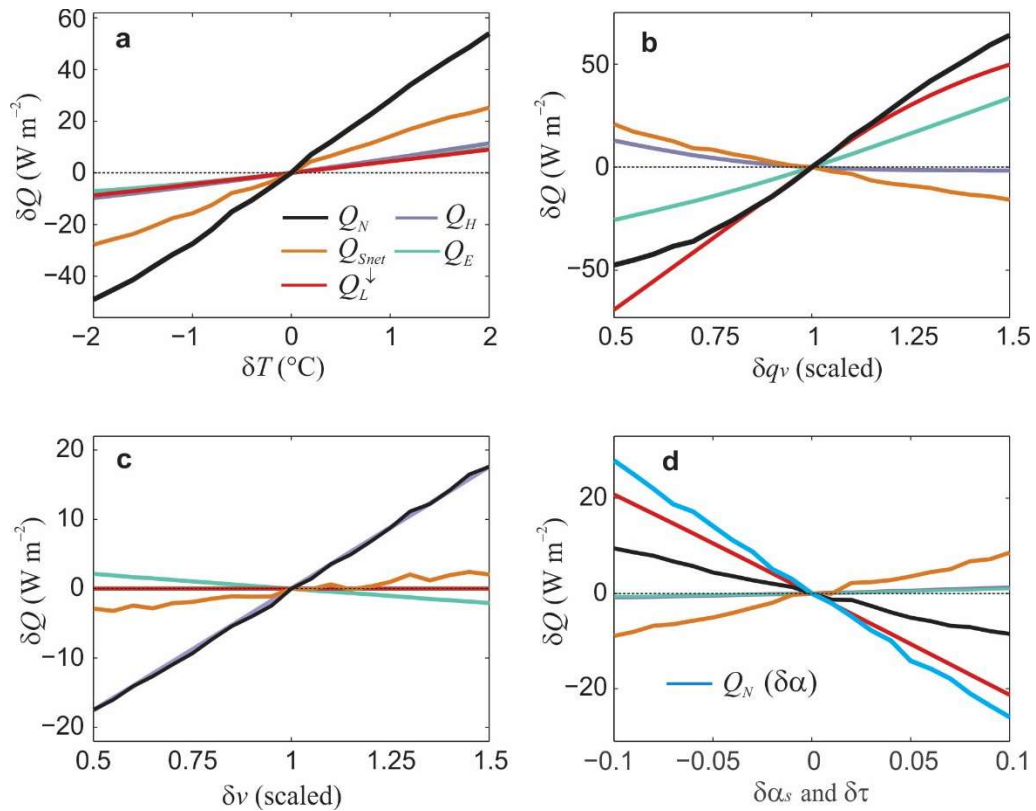
1358
1359
1360 **Figure 6**. Sensitivity of the surface energy fluxes at Haig Glacier to changes in (a) temperature
1361 (case 2), (b) specific humidity (case 6), (c) wind speed (case 7), and (d) atmospheric transmittance
1362 (case 8) and albedo (blue line, case 9). All lines are anomalies relative to the baseline data from
1363 the period 2002-2012, and indicate the mean sensitivity of the different energy fluxes over this
1364 period. Please note the different y (δQ) scales.
1365

1366

1367

1368

37
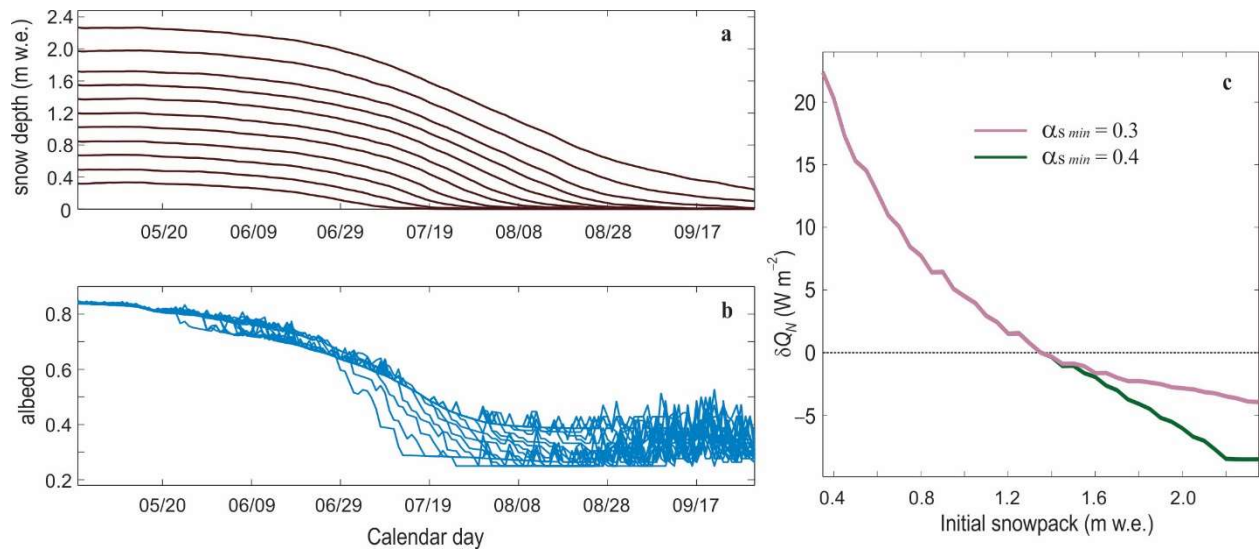
Figure 7. Sensitivity to the winter mass balance, examined by varying May 1 snow depth from 0.36-2.36 m w.e., relative to the reference value of 1.36 m w.e. at the glacier AWS. (a) Snow depth and (b) albedo through the summer melt season, May 1-Sept 30, for the different initial snow depths. (c) Net summer (JJA) energy balance change as a function of the winter mass balance for two different settings of the minimum snow albedo.
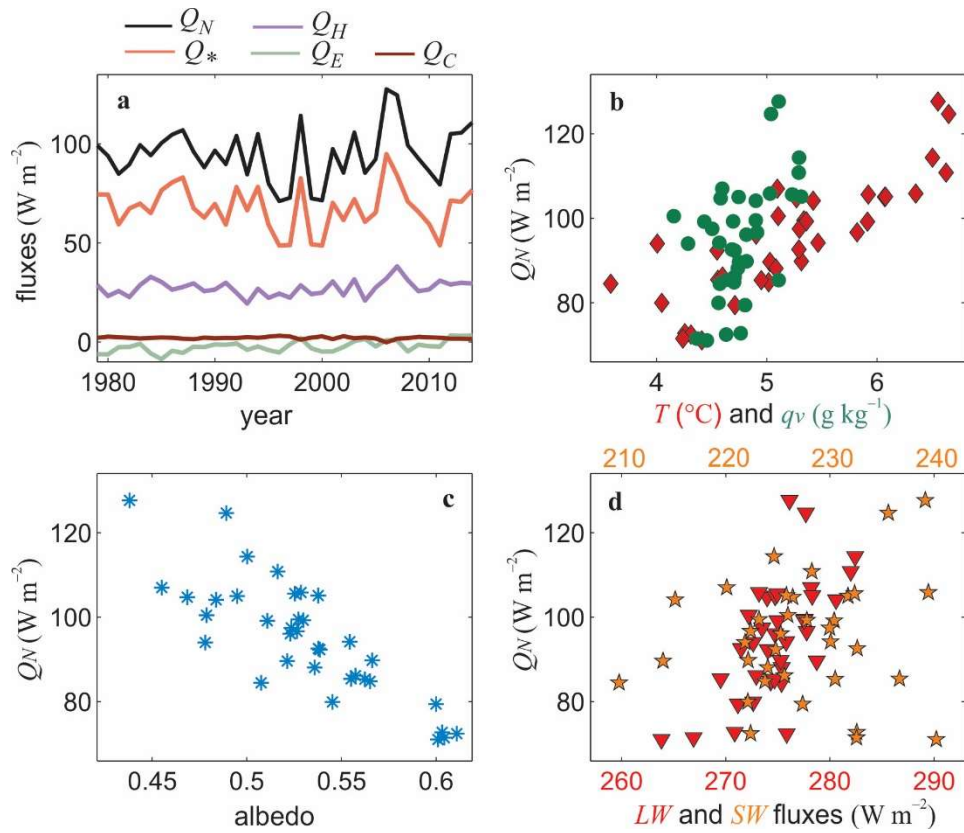
Figure 8. a) Mean summer (JJA) NARR-forced surface energy fluxes at Haig Glacier, 1979-2014. Mean summer net energy as a function of (b) temperature and specific humidity, (c) albedo, and (d) incoming shortwave and longwave radiation. Table 6 gives the associated correlations.
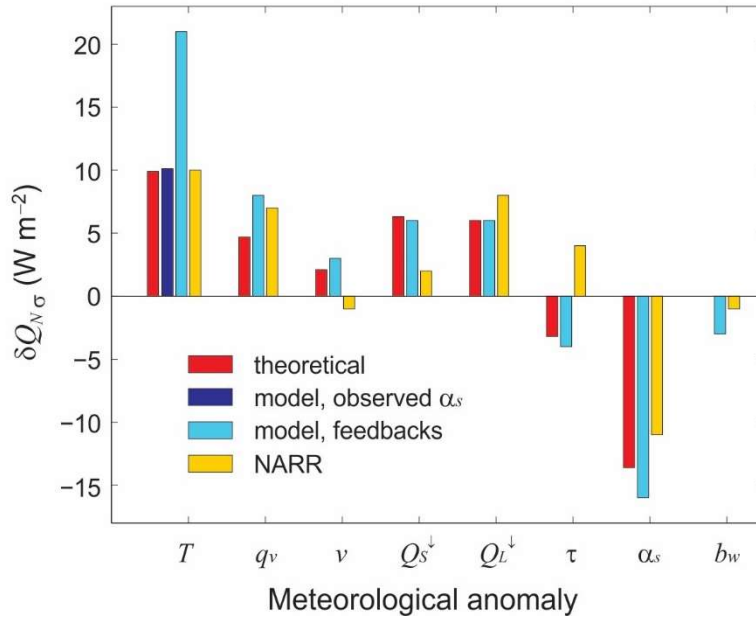
1400

Figure 9. Net energy sensitivity to a 1-σ perturbation in different meteorological variables: comparison of theoretical, *in situ* numerical model, and NARR-based estimates.

1403

1404

1405

1406

1407

1408

1409

1410

1411